UCGE Reports

Number 20269

Department of Geomatics Engineering

Measuring Seasonal Permafrost Deformation with Differential Interferometric Synthetic Aperture Radar

(URL: http://www.geomatics.ucalgary.ca/research/publications/GradTheses.html)

by

Carina Butterworth

April 2008

UNIVERSITY OF CALGARY

Measuring Seasonal Permafrost Deformation with Differential Interferometric Synthetic Aperture Radar

by

Carina Butterworth

A THESIS

SUBMITTED TO THE FACULTY OF GRADUATE STUDIES

IN PARTIAL FULFILLMENT OF THE REQUIREMENTS FOR THE

DEGREE OF MASTER OF SCIENCE

DEPARTMENT OF GEOMATICS ENGINEERING

CALGARY, ALBERTA

APRIL, 2008

© Carina Butterworth 2008

ABSTRACT

Permafrost has been shown as a potential indicator of climate change. Because of the vast area permafrost covers and the remoteness of these areas, a cost effective, remote system is required to monitor small annual changes. Differential Interferometric Synthetic Aperture Radar (DInSAR) has been proposed as a possible tool to monitor small height changes of the surface of the permafrost active layer. Four sets of DInSAR images were processed using three-pass interferometric methods and were factorized into the possible decorrelation components. These components include incidence angles, Doppler centroid differences, ionospheric activity, and coherence. The resulting displacement maps were compared structurally to conventionally surveyed ground truth data and the magnitude was compared with results of a permafrost heave model. One of the four sets of data was found to correspond to the ground truth data and the permafrost heave model. This data set had a high signal to noise ratio (SNR) and low Doppler centroid difference at an incidence angle of 38°. The other sets of data failed to create a reliable differential interferogram. The author concluded that DInSAR shows strong potential as a tool to map permafrost displacement, but further research is required.

ACKNOWLEDGEMENTS

I wish to express my sincere gratitude to my supervisor, Dr. Matthew Tait, for all his encouragement and support throughout the course of my graduate studies. I would also like to acknowledge his help in providing me with the required images and surveyed ground data for the processing and validation of my work.

Thank you to Dr. Michael Collins for accepting me as his student upon the leave of Dr. Tait from the University of Calgary and his advice for completing my thesis.

Davor Gugolj had completed the work on the permafrost heave model and allowed me to use the results for the purposes of validating this thesis work.

Thanks to Dr. Brian Moorman for his advice on interpreting the errors in the images.

Sincere thanks to my dad, Kevin Dunn, for his long hours of assistance in editing.

Financial support came from the University of Calgary in the form of Graduate Research Scholarships, Institute of Sustainable Energy, Environment and Economy, teaching and research assistantships, and personal funding from Dr. Tait. Other financial support came in the form of scholarships from the Graduate Student's Association, Association of Professional Engineers, Geologists and Geophysicists of Alberta (APEGGA), Alberta Heritage Fund, and Alberta Land Surveyor's Association (ALSA). All these are gratefully acknowledged.

To my wonderful, supportive husband, Anthony
And our exceptional son, Karl

TABLE OF CONTENTS

ABSTRACT iii
ACKNOWLEDGEMENTS iv
TABLE OF CONTENTS vi
LIST OF TABLES x
LISTS OF FIGURES xi
NOTATION xiii

1.0 INTRODUCTION 1

2.0 BACKGROUND 2
2.1 Permafrost 2
2.2 Climate Change 4
2.3 Historical Permafrost Monitoring 6
2.3.1 Traditional Differential Precise Leveling 7
2.3.2 Probing 9
2.3.3 Frost / Thaw Tubes 10
2.3.4 Ground Penetrating Radar 12
2.3.5 Electrical Resistivity Imaging 13
2.3.6 Circumpolar Active Layer Monitoring 14
2.3.7 Carrier Phase Differential Global Positioning System 14
2.4 Differential Interferometric Synthetic Aperture Radar 16
2.5 Problem Statement 17

3.0 SYNTHETIC APERTURE RADAR INTERFEROMETRY 18
3.1 Introduction 18
3.2 The Radar Equation 21
3.2.1 Monostatic Point Scatterer Radar Equation 21

3.2.2 Normalized Radar Equation 22
3.2.3 Scattering Properties 23
3.3 Image Geometry 24
3.2.1 Baseline Geometry 26
3.4 Temporal Decorrelation 30
3.4.1 Ionospheric Activity 31
3.4.2 Example of Atmospheric Disturbances 32
3.5 Signal to Noise Ratio (SNR) 33
3.6 Doppler Centroid Differences 34
3.7 Processing Methodology 35
3.7.1 Geometric misregistration 36

4.0 COHERENCE AND PHASE UNWRAPPING 38
4.1 Coherence 38
4.1.1 Imaging Geometry 39
4.1.2 Doppler Centroid Differences and Noise 41
4.1.3 Temporal and Volume Decorrelation 42
4.1.4 Coherence Estimation 43
4.2 Phase Unwrapping 43

5.0 DIFFERENTIAL INTERFEROMETRIC SYNTHETIC APERTURE RADAR 46
5.1 DInSAR Background 46
5.1.1 DInSAR Geometry 46
5.1.2 Differential Interferogram Computations 48
5.1.2.1 Two-Pass Differential Interferometry 48
5.1.2.2 Three-Pass Differential Interferometry 48
5.1.2.3 Four-Pass Differential Interferometry 49
5.2 Objectives 50

6.0 EXPERIMENTAL DESIGN 51
6.1 Data Background 51
6.1.1 Area of Interest 51
6.1.2 Images 52
6.2 SAR Processing 54
6.2.1 Image Registration 54
6.2.2 Interferogram Generation.....58
6.2.3 Coherence Estimation 59
6.2.4 Phase Unwrapping 60
6.2.5 Differential SAR Interferometry.....62
6.2.5.1 ENVISAT ASAR Differential Interferometry.....63
6.2.5.2 RADARSAT Differential Interferometry.....63
6.2.6 Georeferencing.....65
6.3 Ground Data.....65
6.3.1 Conventional Leveling.....65
6.3.2 Permafrost Heave Model 67
6.3.2.1 Thermal Regime Model 67
6.3.2.2 Snow Distribution Model.....68
6.3.2.3 Heave and Subsidence Model.....68

7.0 RESULTS AND ANALYSIS.....70
7.1 Data Input.....70
7.2 Image Registration.....73
7.3 Interferogram Generation.....74
7.4 Coherence Estimation 75
7.5 Phase Unwrapping 84
7.6 Differential Interferometry.....87
7.7 Ground Data Correlation.....95

8.0 CONCLUSIONS AND RECOMMENDATIONS 98
8.1 Conclusions.....98
8.2 Recommendations.....101

REFERENCES 103

LIST OF TABLES

6.1 Data Set Organization 53
7.1 Raw data characteristics of images 71
7.2 Incidence angles and Doppler polynomials 72
7.3 Range and Azimuth Offsets of Image Pairs 73
7.4 Signal to Noise Ratio Statistics 74
7.5 Baselines and their breakdown 75
7.6 Coherence Statistics For Set 1 77
7.7 Coherence Statistics for Set 2 79
7.8 Coherence Statistics for Set 3 81
7.9 Coherence Statistics for RADARSAT 83
7.10 Ionospheric activity recorded in Yellowknife 85
7.11 RADARSAT Signal to Noise Ratio Statistics 92
7.12 RADARSAT Baseline 93

LIST OF FIGURES

2.1 Differences in the types of permafrost and the depths 2
2.2 Northern Hemisphere permafrost coverage 3
2.3 Decreasing Permafrost Regions in the North 5
2.4 Example of conventional leveling with a precise rod (a) and level (b) 8
2.5 Example of a permafrost Probe Rod 9
2.6 Example of a Frost / Thaw Tube 11
2.7 Water Absorption of Radiowaves 13
2.8 Double Differencing GPS 15
3.1 Diagram for the monostatic radar equation 22
3.2 Backscatter power of a group of scatterers in a pixel with dominant scatterers 24
3.3 Image acquisition geometry for a single pixel 25
3.4 Baseline geometry 27
4.1 Example of pixel coherence 39
5.1 Differential interferometry geometry 47
6.1 Picture depicting the landscape and vegetation of the test area 51
6.2 a) Map of the area where the star represents the area of ground truth data and the rectangle is the area of image b; b) Intensity image of the same area where the white square represents the ground truth data area 52
6.3 Flow chart of DInSAR processing used to determine land deformation 55
6.4 June conventional leveling data collection points 66
6.5 Permafrost heave model predicted elevation changes for 2005 69
7.1 a) 17259 & 17760 (June-July) coherence; b) 17760 & 18261 (July-August) coherence 76
7.2 a) 17337 & 17838 (June-July) coherence; b) 17838 & 18339 (July-August) coherence 78
7.3 a) 17302 & 17803 (June-July) coherence; b) 17803 & 18304 (July-August) coherence 80

7.4 a) June / August coherency map; b) August / September coherency map.....82
7.5 a) June / August unwrapped interferogram; b) August / September unwrapped interferogram.....86
7.6 a) Set 1 unwrapped differential interferogram; b) Set 3 unwrapped differential interferogram.....88
7.7 Enhanced image of set 1 differential interferogram 89
7.8 a) Set 1 displacement map; b) Set 3 displacement map.....90
7.9 Colour map used to visualize displacement.....91
7.10 Unwrapped differential interferogram 93
7.11 RADARSAT displacement map 93
7.12 Displacement map of set 1 where blue shows zero subsidence and brown shows 6 cm of subsidence and an enlargement of the area of interest 95
7.13 Differential interferogram of the area of interest with flow accumulation map overlaid 96
7.14 Displacement map compared with the permafrost heave model 97

NOTATION

Symbols

A	differential design matrix including atmospheric parameters
A_a	area of antenna related to gain
α	orientation angle
A_i and B_i	coefficients
$\hat{b}$	baseline direction
B	total baseline
B_A	Bandwidth in azimuth direction
B_p	perpendicular baseline
B_T	transmitted signal bandwidth
$B\perp$	orthogonal baseline projection
$B\perp_{crit}$	Critical baseline (m)
B_r	Data rate (kb/s)
B_{def}	Deformation pair baseline
B_{topo}	Topographic pair baseline
b	function of the image spectral filter
β	beamwidth
c	speed of light
γ_{total}	total coherence
γ_{geom}	imaging geometry
γ_{fdc}	Doppler centroid difference
$\gamma_{process}$	processing methodology
$\gamma_{thermal}$	thermal noise
γ_{volume}	volume of scatterer
$\gamma_{temporal}$	temporal decorrelation
D_p	displacement of the point

Δf_{DC}	Doppler centroid frequency
ζ	Reflected angle (rad)
F_n	receiver noise figure
θ	look angle
θ_i	incidence angle
G	gain
H_p	height of the point
$\hat{h}$	local vertical at the target point
i	iteration count
I	irradiance
K	Boltzmann's constant
L_s	system losses
λ	wavelength
$\|m\|$	magnitude of the motion vector
n	signal's phase shift
$\hat{n}$	unit look vector
P_{ave}	average transmitted power
Pr	power received
Pt	power transmitted
ϕ_p	reference phase
Ω	baseline scaling factor
R	slant range
$R_{xy}(i)$	correlation of two pixels
r_o	complex amplitude of the reference image beam
r(x,y)	master image signal value
$S(\xi_o,\gamma_o)$	Fourier filter plane
T	temperature of receiver
σ	scattering cross-section

σ^o	differential scattering coefficient
V	platform velocity
V	visibility of the fringes
v_{res}	effective velocity of the sensor
$\hat{v}$	velocity variation
W_f	filter size
ϕ_D	phase change
x	pixel in azimuth direction
y	pixel in range direction
*	complex conjugate
<>	ensemble average

Acronyms

ASAR	Advanced Synthetic Aperture Radar
CALM	Circumpolar Active Layer Monitoring Network
DEM	Digital Elevation Model
DGPS	Differential Global Positioning System
DInSAR	Differential Interferometric Synthetic Aperture Radar
DORIS	Doppler Orbitography and Radiopositioning Integration by Satellite
ENVISAT	European Space Agency Environmental Satellite
ERS	Earth Remote Sensing Satellite
ESRI	Environmental Systems Research Institute
FV	Fringe Visibility
GCM	General Circulation Model
GIS	Geographic Information System
GPR	Ground Penetrating Radar
GPS	Global Positioning System
ICC	Intensity Cross-Correlation
InSAR	Synthetic Aperture Radar Interferometry
PCV	Phase Center Variation
PVC	Polyvinyl Chloride
RADAR	Radio Detection and Ranging
RADARSAT	Radio Detection and Ranging Satellite
SAR	Synthetic Aperture Radar
SLC	single look complex
SNR	Signal to Noise Ratio
WGS	World Geodetic System

CHAPTER 1
INTRODUCTION

Climate change has been a topic of interest for many researchers. One of the indicators of interest concerns the response of the permafrost active layer to increasing global temperature. Some of the characteristics of permafrost thaw that have been considered include the magnitude, depth, and rate of the thaw. One measure of these characteristics is relative changes in ground surface elevation. These three characteristics have been evaluated using this measure by means of point-based, conventional methods in places such as Fairbanks, Inuvik, and Saluit. Because of the high cost of these conventional methods, it was important to find a new method to monitor areas as vast as the arctic.

Satellite-based Differential Interferometric Synthetic Aperture Radar (DInSAR) is an active microwave system that can estimate small height variations, considering that the acquired images maintain a high coherence between each other. Unfortunately, because the surface characteristics in the arctic tend to change rapidly during the summer (generally June to August), synthetic aperture radar (SAR) research has not been effective to date because of temporal decorrelation in repeat-pass observations.

Four sets of data were used in this study. The results were analyzed by factoring the different characteristics used in processing the data and the factors affecting temporal decorrelation. One set provided a possible displacement map solution, showing subsidence of up to 6 cm. This map was cropped to a test area of 1 km^2, where ground measurements were acquired. When the ground data and the displacement map were correlated in both structure and amplitude, the results appeared promising.

CHAPTER 2
BACKGROUND

2.1 Permafrost

As concerns about climate change continue to increase and research in the polar regions is becoming more prominent, permafrost monitoring has become an important topic. Permafrost has been defined as ground that remains at or below $0^{o}C$ for at least two consecutive years (Harris et al., 2003). The top soil layer, called the active layer, is the medium that interacts with the atmosphere, causing seasonal freezing and thawing, and therefore varying its thickness over time, distance, and area, as seen in Figure 2.1. Even in apparent homogenous areas, the depth and extent of the freezing and thawing are variable (Nelson et al., 1998a; Nelson et al., 1999; Miller et al., 1998) and are caused by features such as soil texture, soil moisture, and surface vegetation (Hinkel et al., 2001a). These features can also provide a historical record of surface temperature variations (Guglielmin & Dramis, 1999; Nelson et al., 1998b; Nixon & Taylor, 1998; Burgess et al., 2000; Mauro, 2004; Lachenbruch & Marshall, 1986; Beltrami & Taylor, 1994), allowing the study of ongoing trends.

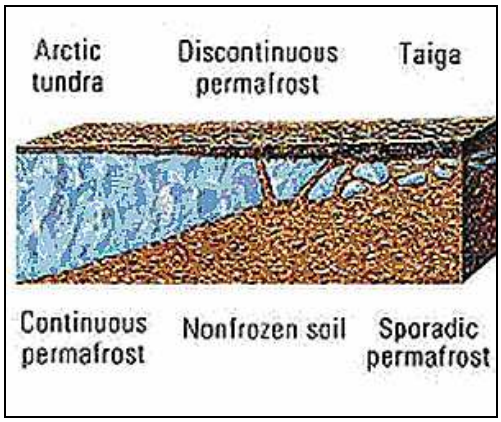

Figure 2.1: Differences in the types and depths of permafrost (Canadian Geographic, 2008)

Permafrost is an important feature of the earth's surface, covering twenty-four percent of it, including twenty-five percent of the Northern Hemisphere's land mass (See Figure 2.2) (Serreze et al., 2000). Thirty percent of all of the world's permafrost can be found in Canada (Zhang et al., 2000). Nearly half of this permafrost is susceptible to global warming. Evidence of permafrost damage has been seen in Western Canada (Serreze et al., 2000; Jorgenson et al., 2001; Romanovsky et al., 2002) and Russia (Pavlov, 1994; Nelson & Anisimov, 1993; Anisimov & Belolutskaya, 2002). Loss of permafrost may result in altered landscapes and damage to infrastructure (Couture et al., 2003; Smith et al., 2005; Ottesen et al., 2002).

Figure 2.2: Northern Hemisphere permafrost coverage in purple (Walker, 2007)

Permafrost variations are important because they potentially indicate climate change (Harris et al., 2003). Monitoring will provide information about the relationship between climate change and permafrost (Davis, 2001; Ishikawa, 2003). Possible characteristics of permafrost that could provide an indication are the timing and rate of the freeze/thaw cycle, the extent of the active layer (Nelson et al., 1993), and the deepening and increasing failure of the active layer (Maxwell, 1997).

There are two major landforms that have been discussed in the literature with respect to permafrost: mountainous regions (Haeberli et al., 1993; Salzmann et al., 2007) and arctic regions (ie. plateaus, deltas, peatlands, etc.) (Laberge & Payette, 1995; Butterworth & Tait, 2007; Nelson et al., 2002). In this study, arctic plateaus and deltas were of specific interest because the effect of climate warming is expected to be greatest in high latitudes (Flato et al., 2000) and approximately 14% of the northern landscape consists of arctic plateaus or deltas. The Mackenzie Delta region was chosen because of the additional interest in oil and gas extraction, which may cause the landscape to subside (Tait & Moorman, 2003).

2.2 Climate Change

Climate change is a complex issue as short term fluctuations have been reported in the past (Osterkamp et al., 1994). Notably, a century-long cyclic change was noted in the 1940s, but following that, a natural global cooling trend stopped and an abnormal warming trend began (Gruza & Rankova, 1980). Increased snow precipitation from 1957 to 2004 and increased annual temperatures from the mid-90s were observed and are believed to be the main drivers for accelerating permafrost thawing (Payette et al., 2004). New temporal changes of the permafrost layer in North America have already been reported (Allard & Rousseau, 1999; Dionne, 1978; Laprise & Payette, 1988; Laberge & Payette, 1995; Thie, 1974). Mackay et al. (1979), Humium (2006), and Brown et al.

(2000) have shown that regions covered by permafrost, such as the Mackenzie Valley and Delta, have been reduced. Figure 2.3 shows the extent of permafrost areas between 1980 and 1999 and the predicted decrease in permafrost by the year 2080.

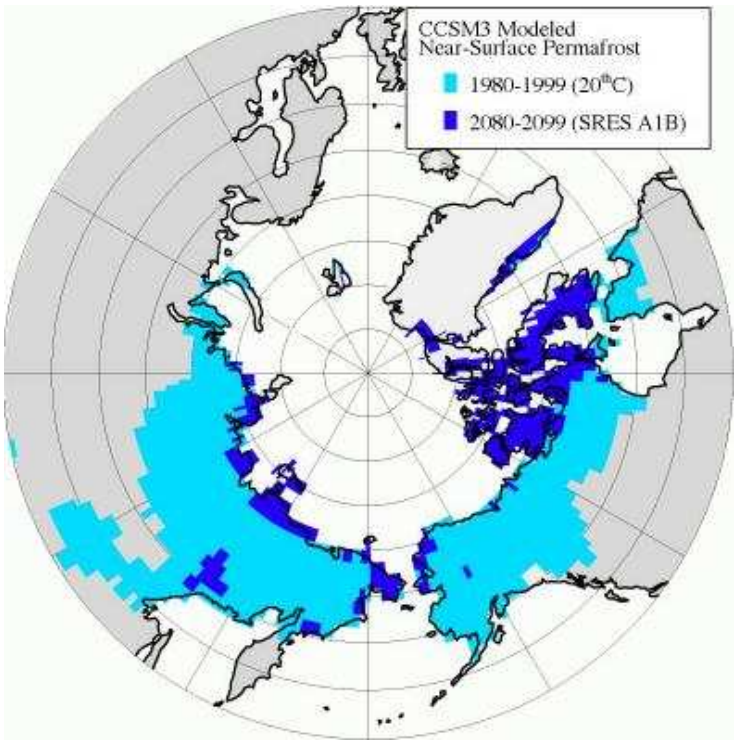

Figure 2.3: Decreasing Permafrost Regions in the North
(National Center for Atmospheric Research, 2005)

There have been recent attempts to model the predicted changes of permafrost due to climate change. Nelson et al. (2002) used a general circulation model (GCM) and permafrost maps to determine the highest danger zones affected by increasing active layer thickness. It was found that the southern limit of arctic permafrost could move 250-350 km north by 2010 (Barsch, 1993). Using climatic, soil, and permafrost interaction data, it was also found that the Canadian southern limit of the permafrost would move 100-200 km north as atmospheric carbon dioxide concentrations double (French, 1996) and that 10 to 17% of the arctic permafrost would be reduced as the active layer would

become 10 to 50% deeper by 2050 (Anisimov & Poliakov, 2003; Janke, 2005). Correlation of air temperatures and permafrost layers has also been used to model permafrost subsidence. In doing so, this method found that there is a strong correlation between ground temperatures and air temperatures (Kakunov, 1999; Oberman & Mazhitova, 2001).

Permafrost soil contains approximately 30% of the world's soil carbon dioxide and as the soil thaws, gaseous carbon and water are released into the atmosphere. The release of these two gases into the atmosphere is predicted to cause a global warming feedback loop (causing an exponential increase in atmospheric carbon dioxide) (Nelson & Hinkel, 2003).

An important aspect of permafrost thaw is the effect on infrastructure, such as the ground deformation affecting the construction of the Qinghai - Tibet railway in China (Zhen Li et al., 2003) or the present infrastructure in Inuvik and Saluit in Canada (Heginbottom, 1973). Because frozen ground contains large quantities of moisture and very poor drainage, thawing creates large pools of water during summer seasons causing soft and unstable soil. This lack of stability causes many problems with infrastructure development and maintenance (U.S. Arctic Research Commission Permafrost Task Force, 2003). Recent warming in Canada has caused buckled highways and destabilized houses. Heave and settlement problems occur as the ice changes temperatures and the particle properties of the soil adjust, therefore changing the foundation stability of infrastructure (USINFO, 2005).

2.3 Historical Permafrost Monitoring

The above events have shown that it is time to start monitoring permafrost layer changes. Because there may only be small centimeter or sub-centimeter level changes of the

permafrost layer on an annual basis, it is important to incorporate a permanent, accurate, and cost efficient monitoring system. There are several methods that have been used in the past:

- traditional precise leveling;
- probing;
- frost / thaw tubes;
- soil temperature profiles;
- Circumpolar Active Layer Monitoring Network (CALM);
- ground penetrating radar;
- electrical resistivity imaging; and,
- Carrier Phase Differential Global Positioning System;

2.3.1 Traditional Differential Precise Leveling

Traditional differential precise leveling (Figure 2.4) is one of the most accurate ways to detect small changes. When a network is arranged suitably, vertical changes can be detected within a sub-millimeter level (Merry, 1998). In most cases, two people are required for the work, where one will use the level and the other will move around with the measuring rod. The post-processing of the data is simply a collaboration and analysis of the measured points.

Unfortunately, there are difficulties with this method in the polar regions. One of these difficulties is the large water bodies scattered throughout the landscape. Traditional differential precise leveling with sub-millimeter accuracies requires site lengths of less than 50 meters to prevent significant atmospheric errors, which can be difficult in such terrains.

Figure 2.4: Example of conventional leveling with a precise rod (a) and level (b)

Stable benchmarks are difficult to find and place (Tait et al., 2004**;** Tait et al., 2005). Without a stable benchmark, only relative measurements can be taken, meaning without any specific reference to an ellipsoid or the geoid. Also, the network needs to be arranged where human access is possible, limiting the number of measurements taken and the size of the monitoring areas.

When presenting precise leveling data, two options are available. The first option is to show a grid of coordinates (Laprise & Payette, 1988). The grid of coordinates with their heights provides point data that can be used later for visualization purposes, but can be limited by interpolation methods. To acquire grid data, points must be taken systematically at regular intervals, which may be difficult to achieve in the north where there are numerous large water bodies. The second option is contour measurements (Laberge & Payette, 1995). The contour measurements can show the levels of subsidence, but the method provides an estimated result, based on the interpolation of individual points. The accuracy depends on the contour interval. Both of these options are limited to a small area and can be costly in expense and time.

2.3.2 Probing

Probing involves pushing a graduated rod into the active layer until the solid ground is felt (the inactive layer). The depth of the active layer is read from the rod graduations at the soil surface. Figure 2.5 illustrates an example of a probe. One person can complete these measurements in an area, but it can be very time consuming. These depth measurements are strictly made relative to the surface (CALM, 2006). The soil properties, including salinity, particle size, and temperature may affect the active layer's depth (Nelson & Hinkel, 2003) and can be used to help calculate the bottom of the active layer.

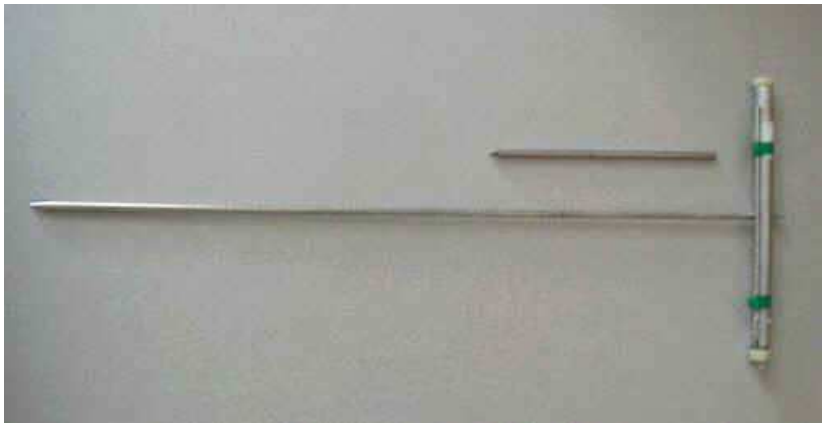

Figure 2.5: Example of a permafrost Probe Rod

If the active layer is thick, the rod needs to be carefully monitored so that the rod material does not bend. The accuracy of the probe is within a few centimeters and is relative. This method is the least expensive method, quick, and easy to use. It is very good for sampling designs, especially when completed in a grid and linearly interpolated between points.

The probe is generally used to determine the temperature of the soil and the soil's moisture (Hinkel et al., 2001b; Mauro, 2004; Smith et al., 2005). These instruments can be found within the probe, allowing for immediate measurement data. It has been found that the active layer thickness depends on the ground surface temperature and the thermal properties of the ground (Guglielmin, 2006), therefore requiring several collection points in one area. Again, this data is only point data, so an interpolation method is required to determine a continuous profile of the active layer. It is also restricted to accessible land and generally covers only a small area.

2.3.3 Frost / Thaw Tubes

When using a frost tube, a hole is drilled or bored perpendicularly into the frozen ground, then a PVC pipe is inserted with a clear plastic tube with inches or centimeters marked inside of it. The clear tube is then filled with a liquid that changes colour when the soil's temperature reaches the freezing point and is then sealed at both ends. When the measurement is to be made, the user pulls the tube out of the PVC pipe to estimate the depth of the freezing point. Most frost tubes are approximately 150 cm long.

The greatest benefit of frost tubes is that they provide an inexpensive annual report of the freezing and thawing of the permafrost active layer. They are also very durable to animal damage and weathering and they remain very stable as a reference point. Where the layer is too deep for probing or the ground is saline, fine-textured, or stony, the frost tubes are ideal because of their stability and durability (Nelson & Hinkel, 2003). Figure 2.6 shows the construction design of the tube and its positioning relative to the ground.

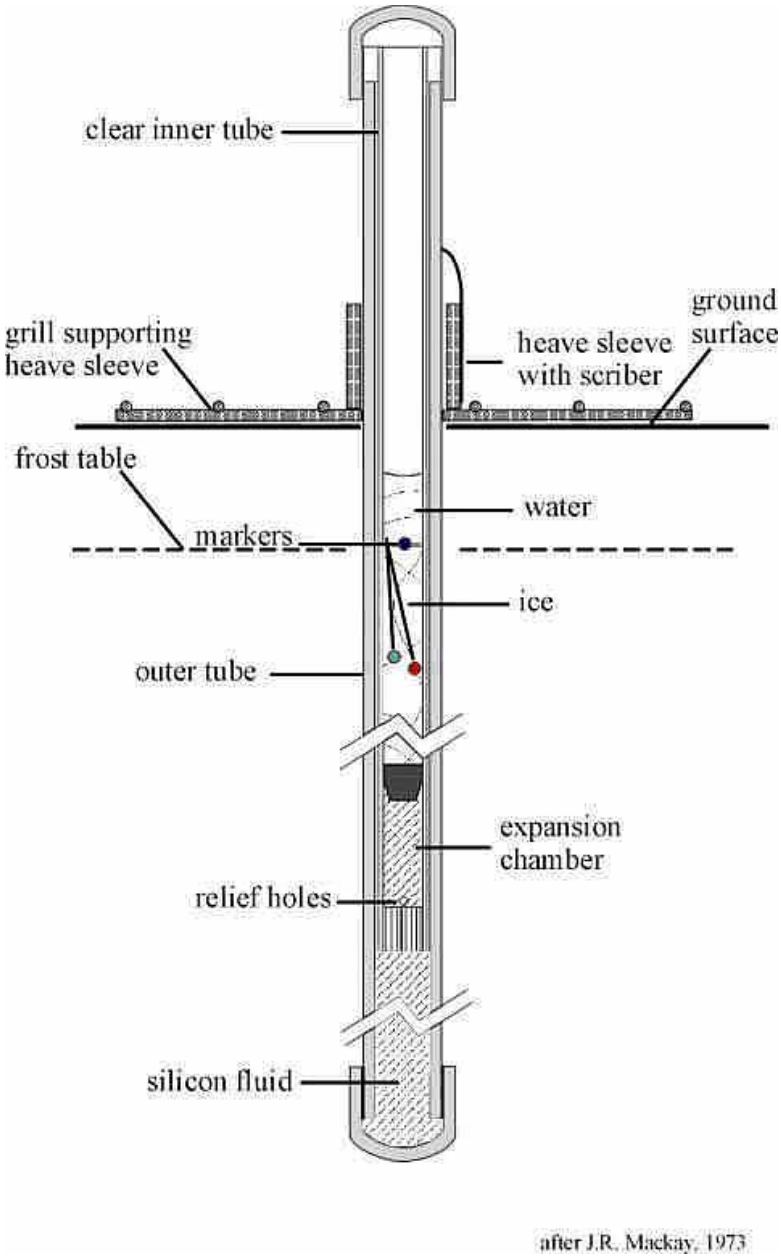

Figure 2.6: Example of a Frost / Thaw Tube

There are two major disadvantages to using frost tubes: accuracy and installation requirements. The information provided by frost tubes does not indicate the exact dates of each of the measurements. This hampers the correlation of the measurements with

temperature trend data. The installation of a single frost tube requires expensive drilling. The drilling generally disrupts the surface of the permafrost causing alterations to the results. Most importantly, the site of the frost tubes needs to be accessible for machinery and humans to install and maintain each tube. Once the frost tube is installed, one person is required to collect the data to create a model of the freezing and thawing of the tube.

2.3.4 Ground Penetrating Radar

Ground penetrating radar (GPR) is a ground based system that can be used to determine the ice's thickness. Ice is transparent to the microwave radio signals, but ice-sediment and ice-water interfaces are reflective; therefore, GPR is most effectively used in the winter in wetland areas.

The properties of permafrost have favourable electrical properties for the use of GPR. When the soil temperature is below 0°C, the conductivity, the dielectric permittivity, and the loss tangent tend to decrease, while the velocity of propagation increases (Scott et al., 1990). These effects mean that the penetration depths also increase, but if there is too much ice in the soil, there is a reduced ability to detect all the features due to scattering losses.

This concept can be seen in Figure 2.7. There are pockets of water that form around the permafrost regions during the summer and because water absorbs electromagnetic pulses, the resulting images would not be useful. Insufficient penetration results because of the water presence during the summer. When GPR is used in the polar regions, it is used based on the theory that the active layer holds less water than the inactive layer (Moldoveanu et al., 2003).

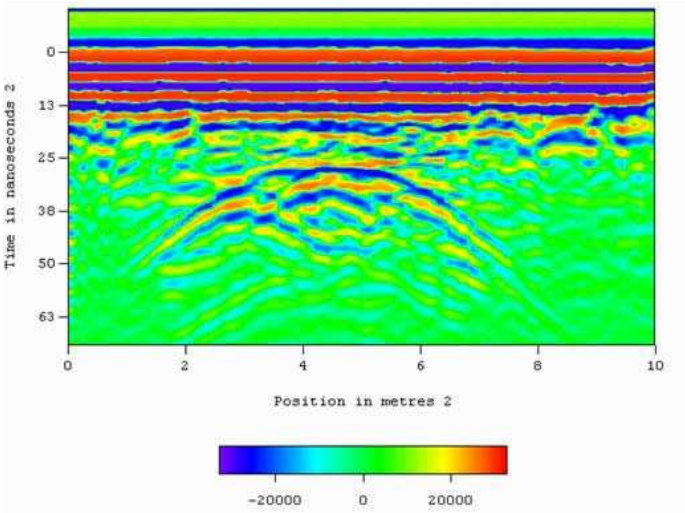

Figure 2.7: Water Absorption of Radiowaves

The benefit of using GPR over and above the previously discussed systems is that the GPR returns a continuous profile that requires no interpolation between points. GPR has been used to study different spatial and temporal changes in the active layer thickness (Wong et al., 1977; Annan & Davis, 1978; Pilon et al., 1979; Pilon et al., 1985; Doolittle et al., 1990; Doolittle et al., 1992; Hinkel et al., 2001b) and probing was used to verify the results. Unfortunately, there is no method today to determine its accuracy with permafrost, but it is believed to be within 15% of the measurements made in fine grain soils (Nelson & Hinkel, 2003). For example, if the layer is 50 cm thick, the measurements may be accurate to 7 cm. The one major disadvantage to GPR is that the equipment is very expensive to purchase and transport, limiting the use to less rugged terrain.

2.3.5 Electrical Resistivity Imaging

One other method that has been used in monitoring permafrost is electrical resistivity imaging (Krautblatter & Hauck, 2007). In the past, it has been primarily used to classify mountain permafrost (Hauck & Vonder Mühll, 2003; Ishikawa et al., 2001; Kneisel,

2006; Kneisel & Hauck, 2003). The idea behind this type of imaging is based on the fact that at the freezing point, there is an increase in the electrical resistivity of the soil. A current is injected into the ground using two electrodes and then the voltage difference is determined. The disadvantages to using electrical resistivity imaging are that any amount of water in the soil will affect the results and that the readings remain relatively shallow (Kneisel et al., 2007). Because arctic permafrost can be hundreds of meters deep and contain a high soil moisture content, this type of monitoring would not be practical.

2.3.6 Circumpolar Active Layer Monitoring

Circumpolar Active Layer Monitoring (CALM) network was established in the 1990's and incorporates probing, frost / thaw tubes, soil temperature profiles, and visual measurements (CALM, 2006). The program originally did not report or archive the data collected, so the available historical measurement data covers only the past three to five years. Now, all the data is freely available and provides ground truth data with approximately 2 cm accuracy (Brown et al., 2000). Linear interpolation is used between each of the points of measurement.

2.3.7 Carrier Phase Differential Global Positioning System

Carrier phase differential global positioning system is also a very useful way of detecting small changes with a millimeter to centimeter accuracy (Tait, et. al., 2004). The system uses the double differential mode while using a nearby reference station (Figure 2.8). If the system is applied on a large scale, such as global permafrost monitoring, several reference stations are required (Varner & Cannon, 2002). Using DGPS in the arctic is beneficial because of the large scale of land and stable height reference stations are not required. Because of the number of large water bodies, DGPS was predicted to be a better

option than conventional leveling (Cramer et al., 1999). But again, the problem arises since the areas to be measured must be accessible.

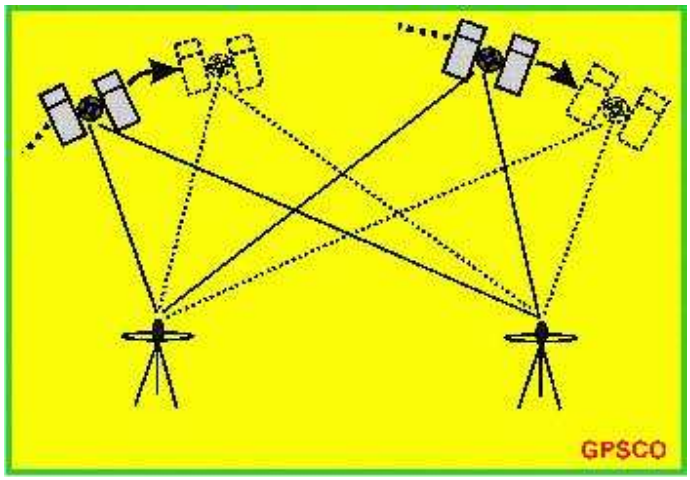

Figure 2.8: Double Differencing GPS

A disadvantage of differential GPS is that a variety of errors need to be corrected or compensated for. A few corrections that directly affect the polar regions are (Varner & Cannon, 2002; Sheng et al., 2007):

- ionospheric activity
- poor satellite geometry
- multipath effects
- phase-center-variation (PCV).

Tait, et. al. (2004) had developed algorithms and methods to reduce these errors to produce the best results. In the processing of the data, the ionospheric activity value was considered ionospheric free (because this method combination helped to reduce the ionospheric errors), an algorithm function provided a map of the troposphere, and a

method was developed to reduce the effect of ionospheric activity, poor geometry, and PCV.

Sheng et al. (2007) found the best accuracy of the DGPS results in the high arctic were around 2mm +- 8mm, when a receiver was left collecting data for 12 hours.

From the above previously used methods, one can see that each of them require direct measurements of the soil. This requires accessibility and appropriate weather conditions to allow for measurements; therefore there are ground observations in only a small portion of the arctic (Little et al., 2003). Another option is to look for remotely sensed data, such as aerial or satellite data. These data will generally provide image coverage of the area, where the spatial accuracy is restricted to the pixel resolution. Remote sensing via airborne or space borne sensors provides the greatest chance for large scale monitoring of the permafrost regions (U.S. Arctic Research Commission Permafrost Task Force, 2003). There are many options available for remotely sensed data, but differential synthetic aperture radar interferometry (DInSAR) was chosen above all the rest. The following section explains the reasoning behind this choice and provides information on the foreseen advantages and disadvantages of this technology.

2.4 Differential Interferometric Synthetic Aperture Radar

DInSAR is another way of monitoring height changes. The first original use of satellite-based DInSAR was to monitor ground motion in agricultural fields by Gabriel et al. (1989) and it uses a repeat pass principle to collect the data. The detectable displacements enter into the sensor directly and therefore can have an accuracy of a fraction of its wavelength. The actual displacement measurement is considered a measure of the temporal decorrelation of each pass's image. Temporal decorrelation can

be defined as the phase difference of two signals that are separated by a period of time. Using these phase differences, one can create a displacement map of a particular area.

The advantages of using DInSAR in the arctic are the accessibility to large areas without the need of repeated human interaction. It also does not have any lasting effect on the environment (for example, pathways built, vegetation damaged, permafrost being altered) and it can remotely monitor large areas without a local point-based system. It is very cost effective because the satellites are already in orbit and the images are available for use.

But there are disadvantages in using DInSAR in the arctic. A few of problems are the rapid changes in vegetation between passes, the ionospheric activity and the tropospheric activity. The processing of the images can be also very difficult.

2.5 Problem Statement

The remoteness and unrelenting harsh environment of the polar regions highlighted the need to find a new, effective remote sensing method. Large area coverage, high spatial resolution, and high vertical accuracy cannot be achieved with the techniques mentioned in section 2.3. To solve these limitations, synthetic aperture radar interferometry (InSAR) has been proposed as an alternative (Graham, 1974; Zebker & Goldstein, 1986). Differential synthetic aperture radar interferometry (DInSAR) showed promise and was chosen for evaluation in this research.

CHAPTER THREE
SYNTHETIC APERTURE RADAR INTERFEROMETRY

3.1 Introduction

InSAR is a technique that uses radar pulse echoes to produce a two dimensional image (Rodiguez & Martin, 1992). Because SAR satellites are active and use microwaves, data can be acquired either day or night and in any weather condition (Rosen et al., 2000). When using temporally separated, repeat-pass InSAR, also called differential interferometric SAR (DInSAR), these radar signals can be used to estimate elevation changes (Hanssen, 2003), soil moisture (Komarov et al., 2002; Mironov et al., 2005), ice content of land (Moorman & Vachon, 1998), be used for heat loss mapping (Granberg, 1994), vegetation classification (Hall-Atkinson & Smith, 2001; Granberg, 1994) or monitor deformation of the ground, as shown in the following four examples of applications.

1. Earthquake Monitoring. After the 1998 Zhangbei-Shangyi earthquake in China, precise seismic deformation measurements became a topic of interest. SAR interferometry was used to show surface deformation. Using the ERS-1/2 SAR tandem mode data taken before the earthquake, the topographic phase signals were reduced significantly (Wang et al., 2004). The resulting image demonstrated the location of the epi-center and the surface deformation after the earthquake resided. Several papers have been written for earthquake monitoring in the past (for example, Fialko et al., 2005; Crippa et al., 2006).

2. Land Subsistence Detection. As the earth's population uses large amounts of subsurface natural materials that are not being replaced as rapidly, the ground surface will settle or sink. In China, land subsistence has been seen in Suzhou City, because

the cities population was using too much ground water (Wang et al., 2004), and a similar effect is taking place in Central Valley, California in the oil and gas fields (Fielding & Dupre, 1999).

3. Volcanic Eruptions. The transition period between a volcano being at rest and its eruption is not fully understood. Using DInSAR, Lu et al. (2002) has found that there are four deformation processes that occur in the transition period. There also is the possibility to monitor lava characteristics, according to Lu & Freymueller (1998). These findings can help provide faster updates regarding the possibility of eruptions and provide a priori information as to the strength of the upcoming eruption.

4. Glacier Motion. There are several mentions of using DInSAR for studying glacier motion, only two are mentioned here (Eldhuset et al., 2003; Strozzi et al., 2002). With concerns regarding the climate change problem, glaciers are among one of the land features greatly affected by temperature changes and are providing information on the rate of climate change.

Radar satellites record the phase and amplitude values of the waves. This information can be used to improve accuracy of determining the magnitude and direction of land deformation. Horizontal and vertical change detection accuracy can be in the millimeter level (Wegmueller et al., 2006), but is usually in the centimeter range (Rodiguez & Martin, 1992).

The most important feature of SAR interferometry is the ability to map remote areas. Larger areas can be monitored directly, without requiring continual human interaction on the land, but because the idea of using SAR interferometry for permafrost monitoring is relatively new, there are some challenges that were involved.

The first challenge when using DInSAR is choosing the appropriate images. Temporal decorrelation and image geometry are two very important attributes to consider when making this decision (Strozzi et al., 2003). During the early summer to mid-fall, there is a better possibility of high coherence of the images in the arctic. Once there is snow on the ground, the images may become inconsistent because of the moisture and density heterogeneities, which are detected by volume scattering of the microwaves. Because the purpose of the project is to determine the surface deformation of the permafrost layer, this is best completed during the summer season, where the surface of the permafrost is unobstructed by snow.

Temporal decorrelation, image geometry, Doppler centroid differencing, and processing methodology will affect the coherence of the image. If the coherence of the image is too low, image registration, phase unwrapping, and the creation of a deformation map will be affected. Also, coherence must exceed a threshold level, which may not be possible in certain situations. Coherence will be discussed in greater detail in the next chapter.

Finally, the field information and the mathematical model of the images are among the toughest challenges. To determine the true permafrost layer, ground elements such as the different types of vegetation and soil elements must be analysed. Also, several ground-based reference stations must be visible in the images to provide geographic coordinates for accurate georeferencing. Atmospheric attenuation and scattering should also be considered while choosing the image processing method and adjusting for random frequency scattering (Foody & Curran, 1994). Unfortunately, with time and financial constraints, the latter was not possible in this study.

The focus of this study is to isolate the above properties and challenges of a differential interferogram and determine the best approach to monitor vertical movement of permafrost. There have been DInSAR permafrost studies in the past (Wang & Li, 1999;

Li et al., 2003), but the results have not been factor analyzed or correlated with ground truth data. The factors spoken about here include temporal decorrelation components, image geometry, and coherence components.

3.2 The Radar Equation

3.2.1 Monostatic Point Scatterer Radar Equation

The governing equation for radar systems is the radar equation. The transmitting antenna sends a signal of known power, then this signal interacts with the target, and finally the receiver antenna measures the amount of returned (or backscattered) signal power. Figure 3.1 provides some insight as how the radar equation works and the following is the monostatic version of the radar equation.

$$P_r = \frac{P_t G^2 \lambda^2 \sigma}{(4\pi)^3 R^4} = \frac{P_t A_a{}^2 \sigma}{4\pi\lambda^2 R^4} \qquad [3.1]$$

Where: Pr = power received

Pt = power transmitted

G = gain

λ = wavelength

σ = scattering cross-section

R = slant range

A_a = area of antenna related to gain.

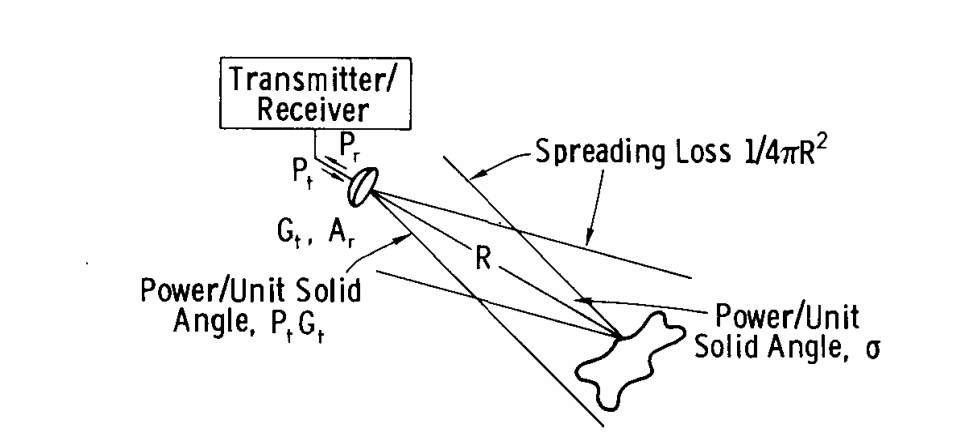

Figure 3.1: Diagram for the monostatic radar equation (Ulaby et al., 1986)

3.2.2 Normalized Radar Equation

The radar equation provided above is only applicable for point scatterers – as mentioned as one of the assumptions; therefore, the scattering cross-section needed to be normalized for unit areas (pixel area). The differential scattering coefficient (also known as the normalized backscatter coefficient) is the average scattering cross-section per unit area and is not dependent on the pixel size. The following equation uses the differential scattering coefficient (σ^o) to determine the total normalized returned power.

$$\overline{P_r} = \frac{\lambda^2}{(4\pi)^3} \int_{pixel_area} \frac{P_t G^2 \sigma^o \delta A}{R^4} \qquad [3.2]$$

Here, σ^o is defined as the differential scattering coefficient. The scattering coefficient is the ratio of the scattering cross section to the area on the ground surface (Woodhouse, 2006). This equation does contain limitations. The first limitation is that it requires many point scatterers over the entire region where G, P_t, and R are constant. Not only this, but it also requires that there are many point scatterers in the illuminated area at any

instant. In this study, these limitations are assumed in the areas of interest and this version of the radar equation was used.

The value of the received power per pixel is affected by many factors that affect the scattering cross-section. A few of these factors that are examined in this study are the image geometry, temporal decorrelation (including ionospheric effects), Signal to Noise Ratio (SNR), Doppler centroid, and processing methodology. These five factors are also used in determining the coherence of image pairs; which was another focus of this study.

3.2.3 Scattering Properties

The radar equation describes the scattering that occurs by a target, therefore an understanding of the term scattering is required. Scattering can be defined as the "redirection of incident electromagnetic energy" (Woodhouse, 2006). Words such as reflection, refraction, and diffraction are more specific types of scattering; where the word "scattering" refers more to the random change of direction created by elements that are the same size or smaller than the wavelength. These elements are referred to as "scatterers."

A measure of the effectiveness of a scatterer is called the scattering cross-section – seen in the radar equation as σ. The scattering cross-section is defined by the ratio of the total scattered power to the total incident power proportionally related to $4\pi R^2$. In an image, the pixel size is the limiting factor here; therefore there is a possibility that the total scattered power can be affected by one dominant scatterer, as can be seen by the bright points in Figure 3.2. Therefore, one of the assumptions of the above radar equation is that the scattering area must consist of randomly placed point scatterers with random amplitudes; and therefore there must not be a dominant scatterer in the pixel.

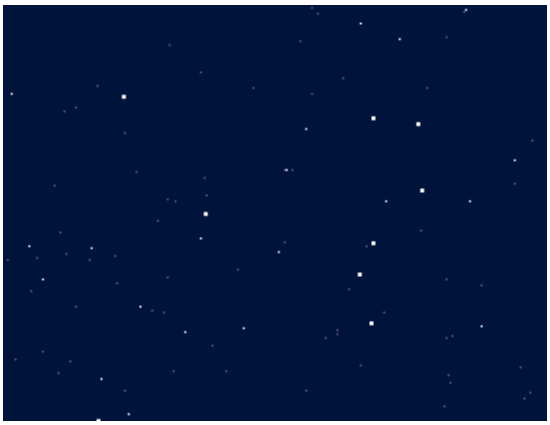

Figure 3.2: Backscatter power of a group of scatterers in a pixel with dominant scatterers

3.3 Image Geometry

Image geometry is of great importance in DInSAR processing, therefore understanding the collection of the data will provide some insight to the physical properties of the signal processing. The signal processing (or focusing) of the data will not be mentioned here because the images used were processed by a third party.

The antenna of a SAR satellite transmits and receives signals at an angle to nadir (the line perpendicular to the earth). This angle is referred to as the incidence angle and is shown in Figure 3.3 (Hansson, 2001) as θ. The incidence angle can be referenced to three different locations: at the near range, the far range, or in the center of the beamwidth (seen as β_r in Figure 3.3). In this study, the incidence angle is considered to be in the center of the beamwidth. There is also another type of incidence angle that is not shown in the figure, which is referred to as the local incidence angle. The local incidence angle is the angle the transmitted signal makes with the ground. Depending on the topography, the local incidence angle can vary greatly from the transmitted incidence angle, creating

problems with foreshadowing, shadowing, and layover. However, in this study, the plateau and delta are relatively flat, decreasing these geometric distortions.

In each acquisition, the incidence angle does not change, but the position of the satellite does, as marked as positions 1 and 2. This change of location creates the early azimuth location and the late azimuth location of the footprint. The near range, far range, early azimuth, and late azimuth define the resolution of the pixel. The azimuth resolution is half the length of the antenna (L_a); therefore, the smaller the antenna is, the better the resolution. The range resolution is determined by the height of the satellite (H_{sat}) and the beamwidth (Hanssen, 2001).

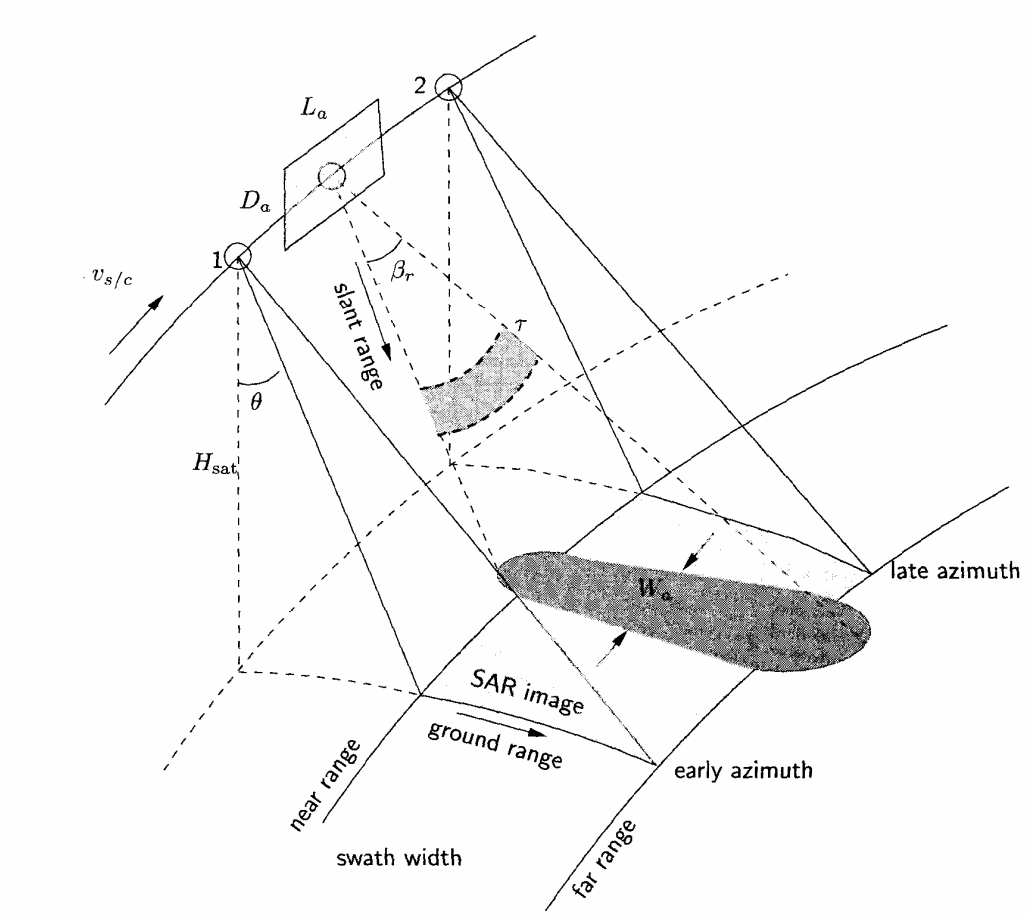

Figure 3.3: Image acquisition geometry for a single pixel

In non-imaging SAR applications, the incidence angle is used to determine information about the radar cross section (Woodhouse, 2006). But in imaging SAR applications, the balance of backscattering power and reduction of geometric distortions (such as foreshadowing, layover, and shadowing) is directly dependent on the chosen incidence angle. An angle of 45° has been previously recommended (Bamler & Hartl, 1998), but in this study, a range of lower values from 28° to 39° had been chosen to enhance the ability to detect vertical change, by keeping the deformation close to the line of sight. It was expected that the signal to noise ratio would be higher for these lower incidence angles because as the angle decreases, the SNR increases. But if the incidence angle is not chosen properly, the returned values of the radar cross-section will change, affecting the coherence between two images.

3.2.1 Baseline Geometry

Once two images of the same area have been acquired, there was one other factor of image geometry to examine: the baseline (Figure 3.4). The baseline is the physical separation of the two satellites while acquiring the same image. The maximum value between satellites that is recommended is 500 m (Li & Goldstein, 1990); otherwise the coherence is reduced. The baselines are dependent on each satellite's individual orbit and therefore cannot be pre-determined.

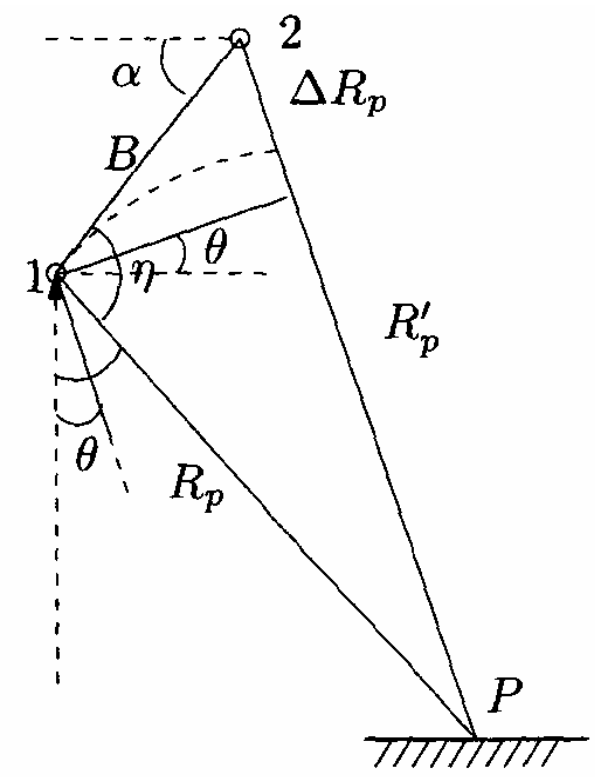

Figure 3.4: Baseline geometry

The radar information must be derived from simple trigonometry by using the distances between two sensors (the baseline) and the resolution cell (the range). In three-pass interferometry, the important factor to consider in the imaging geometry is the baseline correction. In the case of baseline correction, we are examining the spatial baseline because of the high demands on geometric configuration of the interferometric method. The baseline can be used to determine the change in range between the two sensors, but it cannot be used primarily because of the 2π phase ambiguity. If the second sensor is found to the right of the first sensor in terms of flight direction (refer to Figure 3.3), the baseline will be positive and the change in slant range will change from near range to far range.

In developing interferograms, each point / pixel in the image requires a reference phase to correctly register the images. A simple overlay used in image processing would not be sufficient for the complex radar data. Therefore, using the total baseline (B), perpendicular baseline (B_p), the range of the first sensor (R), the height of the point (H_p), the look angle (θ), orientation angle (α), and the displacement of the point (D_p), the reference phase can be determined (Equation 3.3):

$$\phi_p = \frac{4\pi}{\lambda}(B\sin(\theta-\alpha) - D_p - \frac{B_p}{R\sin\theta}H_p) \text{ (Hansson, 2001)} \qquad [3.3]$$

In using this equation in the differential processing, a baseline of 100 meters and a height difference of 1 cm, the phase difference is found to be 127 degrees. This difference is easily detectable in an image. If the displacement is in the line of sight, it is independent of the baseline and can be measured as a fraction of the wavelength. If the baseline is non-zero, as in this study, there is some sensitivity due to the topography.

In the case of a single interferogram, the topographic errors can be determined using the calculated baseline errors. Using least squares estimation and precise orbit data, the following equation was used to calculate the topography residuals:

$$\frac{dh}{\delta B} = -\frac{R(\hat{n}\cdot\hat{b})}{B}\frac{\hat{n}\times\hat{v}}{\hat{b}\cdot(\hat{n}\times\hat{v})}\cdot\hat{h} \text{ (Muellerschoen et al., 2006)} \qquad [3.4]$$

Where $\hat{n}$ is the unit look vector, $\hat{b}$ is the baseline direction, $\hat{v}$ is the velocity variation, and $\hat{h}$ is the local vertical at the target point.

In this study's processing, the baseline between the interferometric pairs needed to be taken into account and scaled. This was done once the reference phase (Equation 3.3)

had been subtracted from both interferograms. The phase observations in the interferogram are considered to be the sum of phase due to distance and the phase due to the backscatter, as long as atmospheric delay is not considered. But in this study, the influence of the atmospheric signal delay must be considered. The atmospheric delay has only one contribution for each pixel in the master (common) image and because the scaling factor (B_{def}/B_{topo}) scales the pair that creates a digital elevation model (DEM) (called the topographic pair), the atmospheric signal is scaled in the same respect. This scaling is important in the analysis of the final differential interferogram and when the unwrapped, scaled topographic pair is subtracted from the remaining pair (called the deformation pair); a differential pair would be created showing only deformation.

The model of the observation equations to calculate the deformation is as follows (Hanssen, 2001):

$$\begin{bmatrix} -\Omega_1 & & & 1 & & \\ & \ddots & & & \ddots & \\ & & -\Omega_m & & & 1 \end{bmatrix} E\left\{\begin{bmatrix} \phi_1^I \\ \phi_2^I \\ \vdots \\ \phi_m^I \\ \phi_1^{wII} \\ \phi_2^{wII} \\ \vdots \\ \phi_m^{wII} \end{bmatrix}\right\} = \begin{bmatrix} A_1 & & & \\ & A_2 & & \\ & & \ddots & \\ & & & A_m \end{bmatrix} \begin{bmatrix} x_1 \\ x_2 \\ \vdots \\ x_m \end{bmatrix} \quad [3.5]$$

Where A is the differential design matrix including atmospheric parameters, which are clearly affected by the baseline scaling factor (Ω). A large scale needs to be avoided otherwise the atmospheric signal is amplified. To reduce the atmospheric signal, the scaling factor must be between zero and one; otherwise the signal will be amplified (Bracewell, 1986). Therefore the topographic pair needs to have these characteristics:

1) a larger baseline than the deformation pair;
2) have a baseline smaller than 70% of the critical baseline; and,
3) contain terrain relief, vegetation, and temporal decorrelation.

In all the sets of data, the June/July pair was used as the topographic pair. In set 3, the topographic pair did not have the longest baseline, which will have amplified the atmospheric delay.

If one is interested in learning more, there are many papers available to provide additional information on this processing (Bamler, 1992; Cumming & Wong, 2005; Hein, 2004; Ulaby et al., 1986).

3.4 Temporal Decorrelation

Temporal decorrelation is defined as differences of the phase and amplitude of the radar signals between passes. It is caused by the radar signal detecting a change in surface properties (also known as the radar cross-section (Wegmueller & Werner, 1995)) or a change in atmospheric / ionospheric effects (Hanssen, 2001) over a particular time period. Northern environments have rapidly changing vegetation because of the short growing season (Billings, 1987). Therefore many changes in the radar cross-section between orbits can be detected. The radar cross-section can be affected by moisture content and dielectric constant values and can cause a phase difference between each acquisition (Woodhouse, 2006). One option to try to improve coherence is to use polarimetry measurements to model the changes in the radar cross-section over time. This option would not only allow for modeling the radar cross-section changes, but would also provide the optimal incidence angle.

Two other factors in temporal decorrelation are the atmospheric and ionospheric changes. As a radar signal travels through the atmosphere, it can be refracted or delayed in each layer. These effects depend on the density of the molecules within each layer. The atmosphere was first reported to be an influential factor on SAR imagery in 1995 by Goldstein (1995), Massonnet & Feigl (1995a), and Tarayre & Massonnet (1996). There are mathematical models available that describe how the atmosphere stochastically affects SAR interferometry (Hanssen, 2001; Massonnet & Feigl, 1995b]; but presently there are no methods available to measure the delay caused by the atmosphere to the required accuracy, spatial resolution, and temporal resolution of this study.

3.4.1 Ionospheric Activity

The ionospheric activity was observed because of the known increased activity in northern environments. The electron density within the ionosphere is often generalized as a spherical shell and is not considered temporally and spatially variable (Hanssen, 2001). High electron activity tends to decrease the range and cause a phase advance of the radar signal because of the interaction with the electrons. A decrease in ionospheric water vapour also tends to increase the range, therefore causing more of a phase advance. Dual-frequency GPS has been used to estimate the ionospheric delay (Hanssen, 2001), but a strong satellite geometry is required (Sardon et al., 1994). It was found that DGPS has a poor geometrical configuration in the Arctic and therefore using DGPS to model the ionosphere is not possible for specific times and locations (Sheng et al., 2007).

The town of Yellowknife, Northwest Territories, has an observatory that provides information on magnetic activity in the ionosphere. This information was collected and analyzed for the purposes of this study. Gray et al. (2000) was the first to prove that ionospheric activity affects the radar signal in the arctic, but the magnitude and validation of this effect were lacking in their study. At this time, the hypothesis used is that the

ionosphere may cause long wavelength gradients over one image, but will not be noticeable in images with a scale less than 50 km.

3.4.2 Example of Atmospheric Disturbances

Hanssen & Feigt (1996) had completed a study to assess if the atmospheric delay in InSAR could be modelled using GPS measurements. The GPS signal was affected by the troposphere in the same way as the radar signal and it was hypothesized that a GPS derived model could be used to quantitatively calculate the signal delay in InSAR. It was found that using GPS to correct the InSAR atmospheric delays was very difficult. The GPS baselines were too noisy and could only be crudely filtered. The correction was also very dependent on the spatial distribution of the GPS receivers. The results of the study also determined that the GPS signal, at a 20 degree elevation, will cover a large area around the receiver; therefore, the gathered data did not provide enough information to remove the small artefacts from the radar signal. In the arctic, the elevation angle is much lower and therefore the atmospheric delay information will cover a much larger area around the GPS receiver. Also, in deformation studies, such as this one, the small scale of deformation could not be determined by the GPS and attempting to filter the SAR interferogram would continue to leave all atmospheric and deformation signals. But, it was found that GPS could be used to parameterize the atmospheric signal in the SAR interferogram. Because of the remoteness of the arctic, it would be difficult and very expensive to set up such a network of GPS receivers and would negate the value of a remote sensing method to monitor permafrost.

3.5 Signal to Noise Ratio (SNR)

The antenna in a satellite system tends to pick up noise from external and internal sources in addition to the image footprint. These noises can come from other microwave sources or from the satellite system itself (such as an electrical leak or a result of the temperature of the instruments) (Woodhouse, 2006). To define the general usefulness of a system, a signal to noise ratio (SNR) is used:

$$SNR = \frac{wanted_signal}{unwanted_signal} \qquad [3.6]$$

So if the SNR is less than one, the system is receiving less useful signal power than noise power, but if the SNR is high, then the system is performing well. The SNR is governed by the radar equation, which relates received power to transmitted power. Often, the radar equation will be seen written in terms of the SNR of the final image to determine the required imaging quality (Cumming & Wong, 2005). When trying to calculate SNR, equation 3.7 can be used:

$$SNR = \frac{P_{ave} G^2 \lambda^3 \sigma^o c}{256\pi^3 R^3 K T B_T F_n L_s V \sin\theta_i} \qquad [3.7]$$

Where: P_{ave} = average transmitted power

G = Antenna gain

λ = wavelength

σ^o = backscatter coefficient

c = speed of light

R = Range to reflector

K = Boltzmann's constant

T = temperature of receiver (K)

B_T = transmitted signal bandwidth

F_n = receiver noise figure

L_s = system losses

V = platform velocity

θ_i = incidence angle

From the equation, one can see that the SNR is inversely proportional to the range of the signal.

When the SNR value is too low, the coherence of an image is affected. This will cause difficulties in registering the images and with phase unwrapping. More information on how the SNR affects the coherence will be discussed later. Unfortunately, the SNR cannot be controlled or predicted in advance and is calculated in the image registration step.

3.6 Doppler Centroid Differences

The Doppler effect occurs in the azimuth direction of the signal footprint. It is proportional to the velocity of the antenna and inversely proportional to the velocity of the radar waves spreading (Hein, 2004). Radar imagery encounters a special form of the Doppler effect called the Doppler centroid frequency. The Doppler centroid frequency is a linear, additive frequency function that communicates the encountered frequency displacement. Once simplified, the Doppler frequency can be calculated by:

$$f_D = 2 \cdot \frac{v_{res}}{\lambda} \cdot \sin \beta \qquad [3.8]$$

Where: v_{res} = effective velocity of the sensor

λ = signal wavelength

β = beamwidth

This equation is a relationship between the beam center location and the returned signal energy in the flight direction (Hanssen, 2001). The Doppler centroid is calculated as the satellite passes through the beam center of the target. This is the point where the acquisition has the maximum gain and can be estimated using a geometric model with the satellite orbit and attitude data. Unfortunately, for the purposes of most research, this method of calculation is not accurate enough. To accurately determine the Doppler centroid, the received signal data is required (Cumming & Wong, 2005) and can only be estimated after the image acquisition.

The difference of the Doppler centroids of two registered pixels is ideally close to zero. As the difference increases, the coherence will decrease (Swart, 2000; Hanssen, 2001). This effect will be discussed in a later section.

3.7 Processing Methodology

Although the processing methodology does not affect the true returned signal, it does affect the quality of the image and the resulting values of the pixels. Errors may result from the chosen method in a processing step. The decorrelation is a result of phase aberrations that can be introduced through spectral misalignment (Bamler & Just, 1993). Spectral misalignment is generally referred to as two images having a phase variance (Bamler & Just, 1993). The images will result in similar scatterers improperly aligned during the processing (Hein, 2004). The misalignment can be a result of two different steps (Eldhuset et al., 2003): geometric misregistration and interpolation methods.

3.7.1 Geometric misregistration

The geometric misregistration can occur in either the range or azimuth direction (Eldhuset et al., 2003). It causes a phase variance and it depends on a displacement of the scatterers (Hein, 2004). If the misregistration is larger than one pixel, the coherence will equal zero; therefore it is recommended that the registration be accurate within at least 1/8 of a pixel (Hein, 2004) before continuing.

In this study, there were two options for image registration: intensity cross correlation algorithm and fringe visibility algorithm. The intensity cross correlation algorithm uses the intensity values of each pixel in the images and correlates them according to the equation:

$$R_{xy}(i) = \sum_{n=-\infty}^{\infty} x(n) \times y(n-i) \qquad [3.9]$$

Where x and y are the pixels to be cross correlated, i is the iteration, and n is the signal's phase shift. The equation overlaps all the elements of the two image's signals and sums everything with the appropriate phase shift. The offset of the intensity peaks shows the phase difference (and therefore the misregistration) for each pixel (Denbigh, 1995). One of the benefits of the intensity cross correlation algorithm is that it allows for any two images to be registered.

The other registration algorithm that was examined was the fringe visibility algorithm. Before using this algorithm, interferometric fringes must be visible in the images. These fringes occur in a 2π cyclic pattern and in the case of radar fringes, the image must exceed the 2π pattern. To determine the visibility of the fringes in each image, equation

3.10 must be used, where I is the irradiance, b is a function of the image spectral filter, and r_o is the complex amplitude of the reference image beam.

$$V = \frac{I_{\max} - I_{\min}}{I_{\max} + I_{\min}} = \frac{2b|r_o|}{1 + b_2|r_o|^2} \qquad [3.10]$$

Once the visibility of the fringes in each image has been determined, Fourier transform integrals are used (Anderson, 1995). Equation 3.11 was used in this study:

$$r(x, y) = \frac{S(\xi_o, \gamma_o)\pi W_f^2 \exp[j2\pi(x\xi_o + y\gamma_o)]}{\lambda R} \qquad [3.11]$$

Where: r(x,y) = the master image signal value

$S(\xi_o,\gamma_o)$ = the Fourier filter plane

W_f = the filter size

x & y = pixel numbers

λ = wavelength

R = slant range

The above equation is then applied to the second image (the slave image) and the fringes are matched. The requirement for this algorithm is that there needs to be an initial interferometric correlation between the two images, which may not be the case in all studies. The fringe visibility algorithm is computationally more expensive and tends to have a very small filter size, only allowing it to cover a few pixels at a time, but because it requires initial correlation between the images, the coherence tends to be higher.

CHAPTER FOUR
COHERENCE AND PHASE UNWRAPPING

4.1 Coherence

Coherence is the measure of the extent to which two reflected radar signals are correlated through phase differences. These values are between zero at low coherence and one at high coherence. In areas of low coherence, problems can arise in creating digital elevation models (DEMs) or interferograms (Abdelfattah & Nicola, 2003). Coherence is affected by several different factors (Zhang & Prinet, 2004; Hanssen, 2001) such as the ones described in the recent sections.

Coherence is a scalar product that consists of six parameters (Abdelfattah & Nicola, 2003) which include:

1) Sensor parameters such as the wavelength, noise, and resolution;
2) Imaging geometry parameters such as baseline and incidence angle in interferometric applications; and,
3) Target parameters, such as volume and temporal changes.

Equation 4.1 presents how coherence can be calculated:

$$\gamma_{total} = \gamma_{geom}\gamma_{fdc}\gamma_{volume}\gamma_{thermal}\gamma_{temporal}\gamma_{process} \qquad [4.1]$$

where: γ_{total} = total coherence

γ_{geom} = imaging geometry

γ_{fdc} = Doppler centroid difference

$\gamma_{process}$ = processing methodology

$\gamma_{thermal}$ = thermal noise

γ_{volume} = volume of scatterer

$\gamma_{temporal}$ = temporal decorrelation

To provide a simpler explanation of how coherence works, Figure 4.1 shows an example of four pixels in an area taken at two different times. Three of the pixels are the same and are therefore said to have high coherence. The bottom right hand pixel is different. If a threshold is set at 0.25 and the two pixels have coherence less than the 0.25, they are considered to have low coherence. Otherwise, if the pixels have coherence above 0.25, they are considered to have high coherence. A couple factors that could cause low coherence are a body of water forming within the pixel area or a rapid change of vegetation.

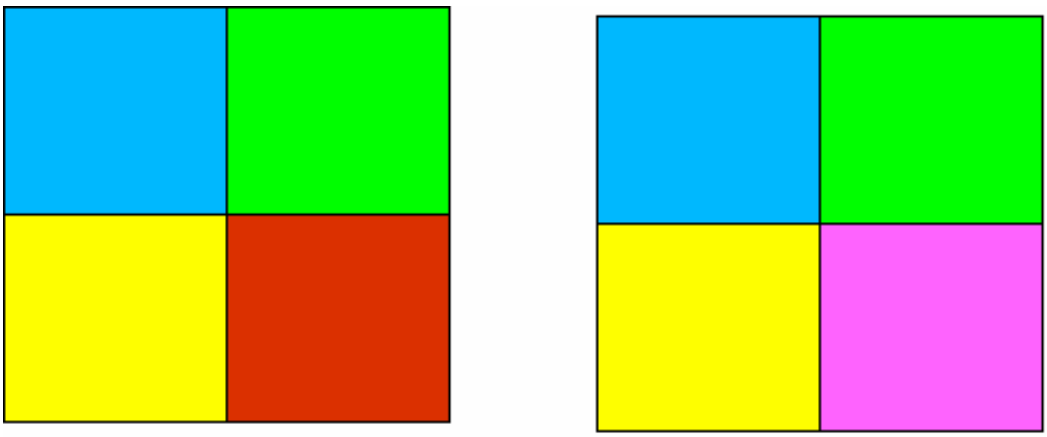

Figure 4.1: Example of pixel coherence

4.1.1 Imaging Geometry

When imaging geometry affects the coherence of a SAR image, it is generally due to the difference in the baseline or incidence angles of two sensors (Hanssen, 2001). When the baseline becomes too long and the spectral shift is equal to the bandwidth, then the two

images will lose all coherence and reliability; but if the baseline is too short, the interferometric technique will lose its ability to calculate three dimensional imagery. To define the maximum length a baseline can be, a critical value must be stated. The critical baseline value can be defined as:

$$B_{\perp crit} = \lambda (B_r / c) R'_p \tan(\theta_{inc} - \zeta) \qquad [4.2]$$

where: $B\perp_{crit}$ = Critical baseline (m)

λ = Wavelength (m)

B_r = Data rate (kb/s)

c = Speed of light (m/s)

R'_p = Slant range (m)

θ_{inc} = Incident angle (rad)

ζ = Reflected angle (rad)

Data rate is defined as the rate information (in bits) can be transported. If the value of the baseline is larger than the critical baseline, the geometric coherence is defaulted to zero (Hanssen, 2001). Using the assumption that the baseline is smaller than the critical baseline value, we can also define the value of the correlation coefficient in equation 4.3 where $B\perp$ is the orthogonal baseline projection of one sensor to the other image's slant range (Li & Goldstein, 1990).

$$\left|\gamma_{geom}\right| = \frac{(B_{\perp crit} - B_{\perp})}{B_{\perp crit}} \qquad [4.3]$$

4.1.2 Doppler Centroid Differences and Noise

The Doppler centroid frequency is related to the azimuth beam center and it locates the azimuth signal energy to provide the best signal-to-noise ratio (European Space Agency, 2006). A difference between the Doppler centroids of two images will cause the coherence to decrease. When the difference of the Doppler centroid is larger than the bandwidth in the azimuth direction, there will be no correlation between the images and, therefore, will equal zero (Hanssen, 2001). Otherwise, the value of the decorrelation can be modeled by

$$|\gamma_{DC}| = 1 - \frac{\Delta f_{DC}}{B_A} \qquad [4.4]$$

where: Δf_{DC} = Doppler centroid frequency

B_A = Bandwidth in azimuth direction

When the average Doppler value is determined in the image during processing, then azimuth filtering is not necessary. But whether filtering is required or not, the effect of the processing methodology on coherence also can be calculated. One way of calculating the coherence of part of the processing methodology is in the coregisteration step, which can be done using equation 4.5, where μ is the relative pixel shift:

$$|\gamma_{process}| = \frac{\sin(\pi\mu)}{\pi\mu} \qquad [4.5]$$

Thermal noise is theoretically determined with the signal to noise ratio (SNR) (Hanssen, 2001) and is determined through the ratio of the signal power (P_r) from the radar

equation (equation 3.1) and the thermal noise power (P_n). Then, using the signal to noise ratio, $\gamma_{thermal}$ is determined to be:

$$\gamma_{thermal} = \frac{1}{1 + SNR^{-1}} \qquad [4.6]$$

4.1.3 Temporal and Volume Decorrelation

As mentioned earlier, temporal decorrelation is one of the biggest problems with InSAR calculations. Unfortunately, because of the number of options and applications of the temporal decorrelation, there is no single analytical model available to describe the correlation coefficient. The best way to approach each application and limit the effect of temporal decorrelation is to collect images with little or no moisture content (SLAM, 2006), use tandem pairs (Knopfle, 1999), or take other measurements, such as GPS measurements, to obtain atmospheric or land deformation information (Rosen et al., 1996). Without these corrections, the SNR and coherence will decrease. In this study, none of these three options for reducing the decorrelation effect were possible; therefore, corrections were not applied.

Volume decorrelation depends strictly on the wavelength of the signal and the scattering mediums (Hanssen, 2001). It is caused by refraction of the radar waves within the target. Again, there are so many different scattering mediums and applications that there is no general analytical model available to describe it. In this study, the volume decorrelation was determined to not have a large effect on the results because of the low vegetation and lack of snow coverage.

4.1.4 Coherence Estimation

Each of the above parameters needs to be calculated for each pixel in an image, and then coherence can be estimated for the pair of images. Coherence estimation windows are commonly used in InSAR processing. They are defined as using a spatial average on a sample coherence area (Zhang & Prinet, 2004). Any biases that are found in an image can be neglected when a large estimation window is used and when the averaged number of the sample coherence estimation satisfies any *a priori* requirements. Here the coherence estimation value is independent of the number of looks. A great way to reduce the coherence estimation variance is to average as many pixels as possible in the constant coherence areas (large coherence estimation window) (Eldhuset et al., 2003).

A small estimation window tends to bias any low coherence values to a high coherence value. The largest problem that arises because of the tendency towards one number is that the discrimination between coherent and incoherent areas will be difficult. So a larger estimation window will help to decrease the bias. Although the larger estimation windows will decrease the absolute coherence values and the range resolution, the data will become more reliable (Hanssen, 2006). But if the estimation window is too large or if the area is not homogenous, too much information will be lost or the final coherence value of the estimation window could be poorly located in comparison to the true image values (Elhuset et al., 2003).

4.2 Phase Unwrapping

One of the most sensitive steps of DInSAR processing is the phase unwrapping step. Phase unwrapping converts the observed relative phase signal which has a 2π modulus interval of $[-\pi, \pi)$ to the unknown absolute phase signal. It is for this step that poor

coherence, low SNR, poor registration, and poor image filtering will become a problem. Phase unwrapping depends on the wrapped fringes created when the interferogram was generated. The error in phase unwrapping comes from the miscounts of the fringe order; therefore quality input and using the appropriate algorithm is essential for quality results (Gutmann & Weber, 2000). A wrapped interferogram displays repetitive phase fringes in an order of 2π. When a phase unwrapping error occurs, fringes are missed or counted more than once.

There are many different phase unwrapping algorithms available. They can be separated into two groups: path-following methods and minimum-norm methods (Ghiglia & Pritt, 1998). The most commonly used methods are the path-following methods, especially the Goldstein's branch cut algorithm (Gutmann & Weber, 2000). The Goldstein's branch cut algorithm is controlled by phase discontinuities; otherwise known as residues (Goldstein et al., 1988). A path is formed by connecting an equal number of negative and positive discontinuity sources using a pairwise connection (Gutmann & Weber, 2000). Neutral discontinuity sources (neutrons) are used to direct the pathway through the negative and positive sources. These connection lines are referred to as branch cuts pointing from positive to negative sources. The connection lines continue through a 2π cycle until there are an equal number of positive and negative sources, to make the path neutral. The unwrapping algorithm is then not allowed to cross these connection lines.

The connection line formation does not have a unique solution; therefore a set of criteria are required to create a repeated answer. One of the criteria is to decide on a minimum cut length threshold (Cusack et al., 1995). Another criterion is to use a low-pass filter separately on each the cosine and sine sections of the phase wave to reduce the number of object discontinuities and increase the SNR (Ghiglia & Pritt, 1998; Winter et al., 1993). The minimum cut length threshold is the simplest criterion to implement of the two

options. Creating the connection lines is the most time and computationally expensive part of creating an interferogram, therefore simpler computations are generally adopted.

Once the connection lines are created, then the image can be unwrapped. The unwrapping occurs along these lines, starting from the positive source to the negative source. Then, to create a continuous image, bridges are created and are placed over the connection lines. This step allows the algorithm to unwrap areas that did not have connection lines, creating a fully unwrapped image.

CHAPTER FIVE
DIFFERENTIAL INTERFEROMETRIC SYNTHETIC APERTURE RADAR

5.1 DInSAR Background

Once phase unwrapping is successful for each interferogram, differential interferometric processing can begin. It is at this point where one can attempt to detect the vertical change in land surface. To visualize how DInSAR works, one can imagine two temporally separated images traveling along the same orbit path (baseline = zero). When subtracting one image from the other and if the land surface height has not changed within fractions of the wavelength, the difference will be zero. If there was a change in the land, there will be a phase difference detected.

5.1.1 DInSAR Geometry

Figure 5.1 (Woodhouse, 2006) show the geometry of DInSAR. The important factor to examine is the change in slant range, given by:

$$D_R = |m| \sin(\theta_i - \zeta) \qquad [5.1]$$

where $|m|$ is the magnitude of the motion vector and ζ is the direction of the motion vector from the horizontal.

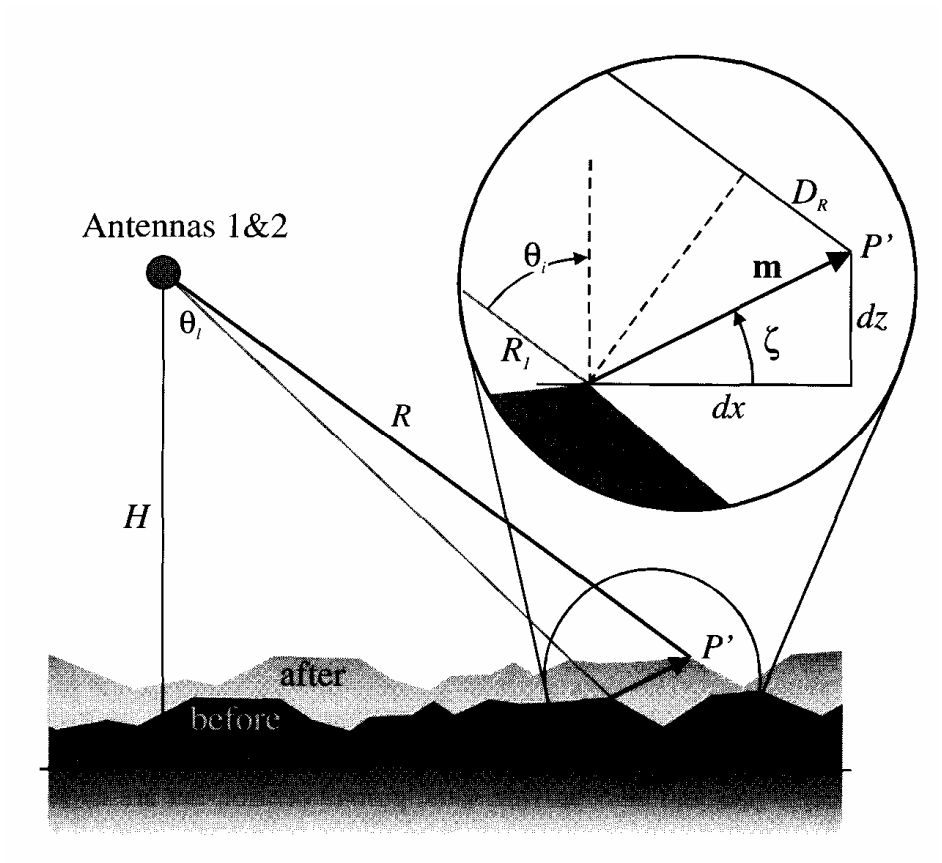

Figure 5.1: Differential interferometry geometry

As mentioned, the surface only needs to move a fraction of the wavelength. Wegmueller et al. (2006) found that in certain conditions, a displacement map can be made with a sub-centimeter accuracy. Equation 5.2 shows this is possible:

$$|m| = \frac{\lambda \phi_D}{2\pi \sin(\theta_i - \zeta)} \qquad [5.2]$$

where ϕ_D is the phase change.

If there is a consistent phase change over the surface and if the area of the ground movement is found to be larger than the coherence estimation window, the coherence will remain high (Woodhouse, 2006). Otherwise, the small phase changes found within a coherence estimation window will decrease the overall coherence values.

5.1.2 Differential Interferogram Computations

There are three options available for computing a differential interferogram: two-pass, three-pass, or four-pass interferometry.

5.1.2.1 Two-Pass Differential Interferometry

Two-pass differential interferometry uses one interferogram and relates the interferogram to a previously calculated DEM. The DEM has to be accurate to about 30 meters in the height direction to be used; therefore GTOPO30 and SRTM data can be used. Thirty meters is considered accurate enough because the DEM is used only as a reference for each pass. The objective of two-pass DInSAR is to determine the difference between each pass with respect to the DEM. There are several examples of two-pass interferometry in literature, such as monitoring earthquakes (Zhang & Cheng, 2005), volcanoes (Lanari et al., 1996; Stevens & Wadge, 2004), and glaciers (Rao et al., 2004). This technique is the most robust and accurate technique, when there is a DEM available (Zhen et al., 2003). If there is not a DEM available, there is a possibility to use three-pass interferometry.

5.1.2.2 Three-Pass Differential Interferometry

Three-pass differential interferometry uses three images, which are converted into two interferograms, with one common reference image (also known as the master image).

One of the requirements of this method is there cannot be any deformation between two of the images or that there is a constant rate of change between all three images. If there is no deformation found between two of the images, the resulting interferogram is called the topographic image. Otherwise, the pair of images with the longest baseline is referred to as the topographic image. In this study, it was found that the deformation had a constant rate of change using the permafrost heave model. More information on this can be found in section 6.3.2.

The other interferogram is called the deformation image and is used for the calculation of the total deformation. These two interferograms are then registered with each other and the phases are subtracted from one another. This creates the differential interferogram. The benefit of using three-pass interferometry is that a DEM is not required for the processing. Because the interferograms need to be registered, the coherence is required to be higher than in two-pass interferometry; otherwise they may not register together properly. Also, both interferograms need to be unwrapped before being taken any further. There are not as many applications of three-pass interferometry; it has been used in mining subsidence applications in the past (Carnec & Delacourt, 2000), which is similar to this study.

5.1.2.3 Four-Pass Differential Interferometry

Another common option for DInSAR processing is four-pass interferometry. In four-pass interferometry, four radar images are used to create two interferograms, but only the first interferogram is unwrapped. This interferogram is required as the topographic estimation so it cannot contain any deformation (Zhen et al., 2003). In a subsidence application, this may be difficult to achieve.

5.2 Objectives

This study is a feasibility study that will help to assess the use of DInSAR in monitoring permafrost subsidence at centimeter accuracies. In this study, three pass differential SAR interferometry is used to determine the subsidence of permafrost in the MacKenzie Delta & River Valley region to a centimeter accuracy. DInSAR is capable of sub-centimeter accuracies, but because of the temporal decorrelation and unaccounted atmospheric effects, it is expected to see a bias. Field observations occurred during the same time period as the radar image acquisitions. These field observations include conventional leveling and data collection for a permafrost heave model, including soil moisture, soil content sampling, and surface temperatures and are to be used in determining the accuracy of the remote sensing application.

If proven possible, DInSAR can be used as a seasonal measure and as a monitor for permafrost subsidence.

The following are the objectives of this study:

1. Create four displacement maps with centimeter accuracy from the radar images;
2. Correlate the pre-calculated conventional leveling DEM and the permafrost heave model with the radar displacement maps; and,
3. Analyze the factors that caused errors in the DInSAR results.

If one of the DInSAR images provides a displacement map that is verified by ground data, then using a factor analysis, the optimal conditions for monitoring permafrost subsidence due to climate change using DInSAR can be determined.

CHAPTER SIX
EXPERIMENTAL DESIGN

6.1 Data Background

6.1.1 Area of Interest

The area of interest was located on the plateau, approximately 500 feet above the MacKenzie Delta by Reindeer Station. In this area, the surface was discontinuous tundra and covered with cotton grass (Figure 6.1). The permafrost is continuous and the entire permafrost layer, including the active layer, can be up to 600 meters deep. Because of the discontinuity of the surface, conventional survey techniques were difficult to use to create a surface model, therefore another method was also required.

Figure 6.1: Picture depicting the landscape and vegetation of the test area

Ground data were used to help determine the reliability of the DInSAR results. The test site can be found at 68.684˚N, 134.084˚W and was a 1 km x 1 km square. It was located approximately 50 km north of Inuvik in the MacKenzie Delta and River Valley (Figure 6.2). The land within the test site consisted of rolling hills with approximately 25 m relief.

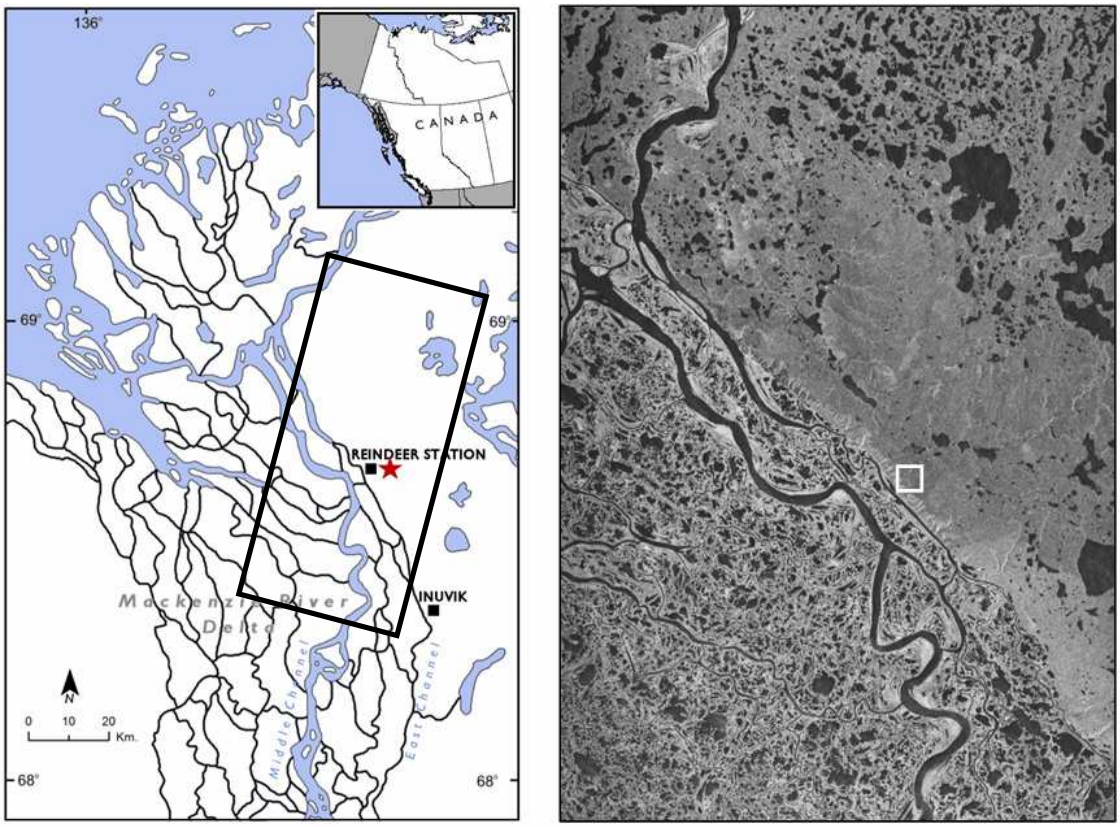

Figure 6.2: a) Map of the area where the star represents the area of ground truth data and the rectangle is the area of image b; b) Intensity image of the same area where the white square represents the ground truth data area

6.1.2 Images

For the purposes of this work, nine images from the Advanced SAR (ASAR) sensor on ENVISAT and three RADARSAT-1 images were used. All 12 single look complex (SLC) images were acquired between the dates of June 18, 2005 and September 8, 2005 and were all in descending node with a frequency of 5.3310044e+009 Hz. The ENVISAT ASAR images were separated into triplets, with 501 orbits or 35 days between each image. Table 6.1 shows how each dataset was separated. The images were chosen

with two common characteristics: the images incorporated a significant part of the permafrost thaw season in 2005 and the test site was centrally located in the images. To optimize the ability of SAR to detect vertical movement, the lowest possible incidence angles were used. Incidence angles varied from 28.7^{o} to 38.5^{o} and were used to investigate how the change in incidence angle would affect the results.

Table 6.1: Data Set Organization

Set	Dates	Orbit Number
ASAR 1	June 18, 2005 July 23, 2005 August 27, 2005	17259 17760 18261
ASAR 2	June 24, 2005 July 29, 2005 September 2, 2005	17337 17838 18339
ASAR 3	June 21, 2005 July 26, 2005 August 30, 2005	17302 17803 18304
RADARSAT	June 28, 2005 August 15, 2005 September 8, 2005	N/A

To improve the baseline estimation of the ENVISAT ASAR orbits, the DORIS (Doppler Orbitography and Radiopositioning Integration by Satellite) precise orbit files for each image were also downloaded from the European Space Agency website. DORIS is a radio frequency tracking system that is based on the Doppler principle. The files provide real-time orbit information including the precise attitude, orbit control, and an atomic time reference.

When choosing these images, there were two different landforms of interest. Each image consisted of the plateau, where the ground truth data was taken, and the active delta. The delta was of interest because of present and planned commercial gas extraction that may lead to additional subsidence of the land. If the differential interferogram is successful in the delta, DInSAR could be used as a potential long term monitoring tool for many companies. The plateau was used as a dry land comparison. Each of these landforms represents approximately 7 – 8% of the arctic region.

6.2 SAR Processing

A thorough investigation was completed to acquire the most appropriate software for radar interferometry processing. Most of the software packages investigated were found only to complete up to the unwrapped interferogram step and did not do differential interferometry. The most appropriate software found was a trial version of Gamma software, created by GAMMA Remote Sensing (Wegmueller et al., 2007). The following sections describe the steps used in the processing and how the results of the processing were validated. Figure 6.3 is a flow chart of how the images were processed.

6.2.1 Image Registration

The first step in image registration was to set the size of the registration estimation window and determine the most appropriate offset estimation algorithm. When two images are acquired, they usually contain an offset in both the azimuth and range direction. It is necessary to correct for these offsets to create a registered pair. Other factors also needed to be assigned, such as the signal to noise ratio (SNR) threshold and multi-looking values.

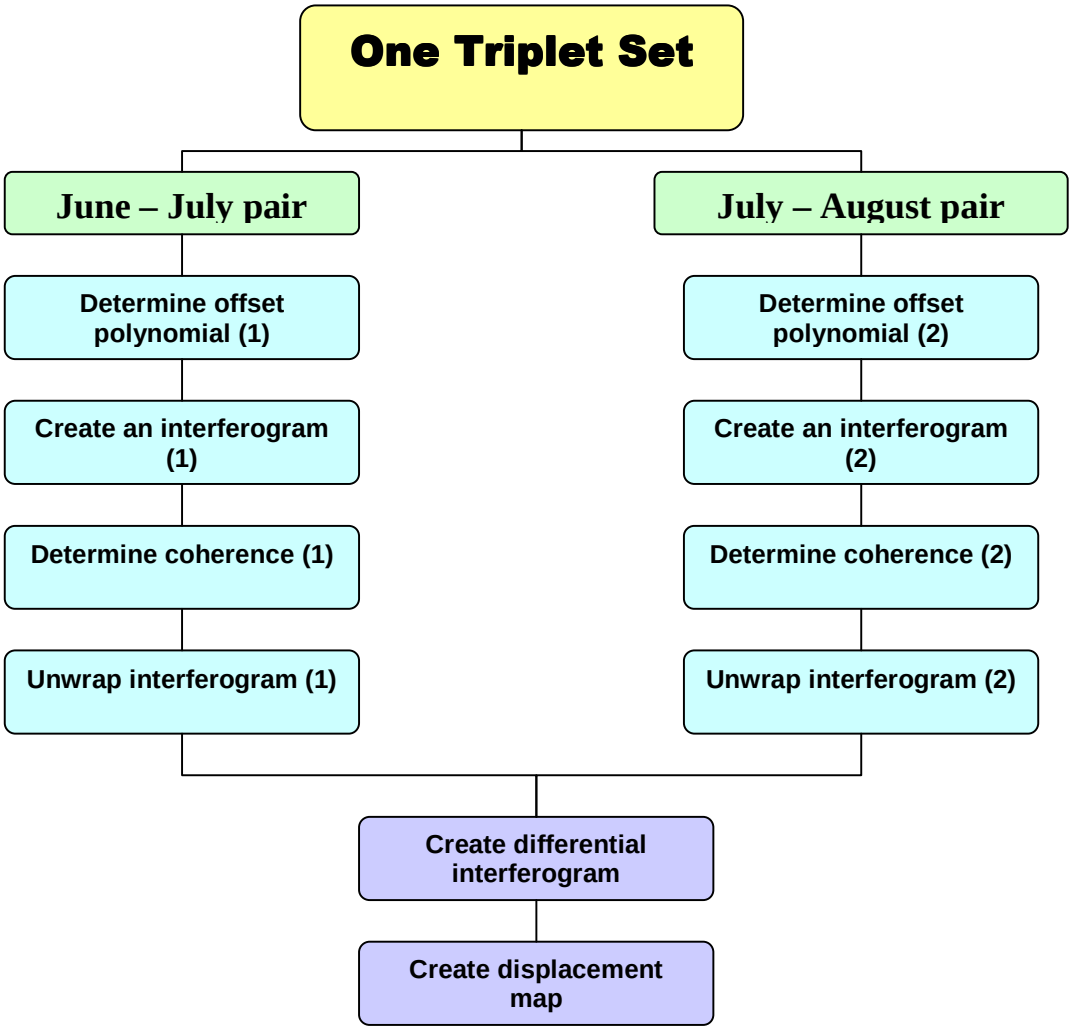

Figure 6.3: Flow chart of DInSAR processing used to determine land deformation

There were two algorithms available: the intensity cross-correlation (ICC) algorithm and the fringe visibility (FV) algorithm. ICC was chosen for this task over FV because ICC allows for the two images to be co-registered, even if they lack interferometric correlation and ICC works very well with natural landscape such as the area of Reindeer Station. The FV algorithm is computationally-time expensive and only samples a small number of points at a time, where the ICC is much faster and can sample a user defined number of points (must be to the power of 2). With the least squares adjustment, a test for the highest average SNR value was run for all images and it was found that the ICC was an average of 0.03 pixels more accurate than the FV algorithm. The decrease in accuracy with the FV algorithm may have been a result of low a priori interferometric correlation between the images.

Two factors, SNR and multi-looking values, were also assigned. The signal to noise ratio (SNR) threshold was set to 7.0. This value was thought to be high enough to eliminate any noise-induced anomalies. The average SNR values were found to be between 8.0 and 10.0, so setting 7.0 as the threshold would still include about 90% of the data. As for the multi-looking value, it was decided to multi-look the range once and the azimuth five times. The 1:5 range to azimuth ratio was recommended by Hanssen (2001) to yield a square pixel. The azimuth magnitude was approximately five times the magnitude of the range, so the azimuth was multi-looked at this point to help improve visualization of the data and reduce azimuthal distortions. The 2:10, 3:15, 4:20 and 5:25 ratios were attempted and it was found that the SNR value decreased linearly; therefore, the 1:5 ratio was used.

Cropping each image to the area of interest was attempted to see if the results would be more accurate. The hypothesis of doing this was to see if limiting the area to fewer water bodies and less terrain differences would help improve registration accuracies. When this was attempted using all pairs, it was found that the full images, not the cropped image,

provided higher accuracy in estimating the pixel offsets. The pixel offset errors of the cropped images were caused by the software having inaccurate georeferencing within each image.

The second step of image registration was to extract the orbit information from the images and compute the offset of the slave image to the master image. In this step, it was determined using tie points within the images that they were skewed in geometry and therefore were adjusted using a simple polynomial for this transformation. Then, the two-dimensional cross-correlation function was used to find the true relative offset by calculating the peak correlation. The relative offset was established at this peak value.

The offset was then adjusted to subpixel accuracy using the ICC algorithm. The algorithm uses an estimation window, size 32 by 64, to correlate the slave image to the master image coordinates. Larger window sizes were tested as recommended by Wegmueller et al. (2007) but they were found to lower the SNR values; therefore, the window size of 32 pixels by 64 pixels was found to keep the highest SNR values.

Finally, once the precise offsets were established, a linear least squares polynomial was designed to model the range and azimuth offsets. A third order polynomial was chosen to create the best global fit and to improve the SNR of the pair. The least squares computation removed any offsets that appeared to be in error and removed the low SNR values; therefore creating a global fit model for the range and azimuth offset polynomials. The accuracy obtained by the least squares estimation of less than 0.2 pixels kept the registration errors below ten percent. The polynomial has the form of:

$$\begin{aligned} range_offset &= A_o x + A_{1range} x^2 + A_{2azimuth} x^3 \\ azimuth_offset &= B_o y + B_{1range} y^2 + B_{2azimuth} y^3 \end{aligned} \qquad [6.1]$$

Where A_i and B_i are the coefficients to be determined, x is the corresponding pixel number in the range direction of the master image, and y is the corresponding pixel number in the azimuth direction of the master image. Once the offset polynomials were determined, the slave image was coregistered to the master image. A two-dimensional *sinc* interpolator was used to resample the slave image to the master image. The interpolator adjusted the geometry of the slave image for the best possible registration.

6.2.2 Interferogram Generation

Before the interferogram was calculated, two radiometrically calibrated intensity images were produced from the master and slave images using the software. These two images were overlaid as landscape references on the calculated complex images and were later used for calculating coherence.

Then, after registering the images, the complex interferogram was generated using the following equation:

$$w_im = \frac{< slc1slc2^* >}{< slc1slc1^* >< slc2slc2^* >} \qquad [6.2]$$

Where * represents the complex conjugate and <> represents the ensemble average of the complex data and the complex conjugate. This equation will calculate the wrapped interferogram pixel by pixel. Also, in this step, a range spectral shift filter and an azimuth common band filter were applied. The range spectral shift filter accounts for the spectral shift due to the changes of local incidence angles between the two images. These incidence angle changes are normally caused by the length of the baseline. The azimuth common band filtering keeps the common frequency between the two images and rejects the other frequencies. This filter is applied to optimize the correlation between the two images by keeping a common band.

To implement the range spectral shift filter, the baselines of the image pairs had to be calculated. The baselines were determined in range, azimuth, and altitude state vector directions and the results were presented as a first order polynomial. The DORIS precise orbit files allowed for accurate calculation of the baseline. This information was further used in removal of the global phase trend and the determination of the landscape heights.

Once the baseline polynomial was known, the flat-Earth phase trend was removed. The trend was determined by the parallel component of the baseline to the look vector of each range swath. This trend could cause errors in the correlation function and the phase unwrapping steps and therefore had to be removed to create a flat-Earth model.

6.2.3 Coherence Estimation

The coherence of the two images was determined by including the complex, flat-Earth interferogram and both intensity images. A coherence estimation window of 5 pixels by 5 pixels was used to maintain the required smoothing of the complex phase information and to enhance the accuracy of the triangular weighting scheme. It was found that slightly larger coherence estimation windows reduced the average coherence by 0.1. The triangular weighting scheme was calculated using a linearly decreasing value with the increasing distance from the center pixel. Following is the coherence estimation window weighting scheme:

0.057 0.255 0.333 0.255 0.057
0.255 0.529 0.667 0.529 0.255
0.333 0.667 1.000 0.667 0.333
0.255 0.529 0.667 0.529 0.255
0.057 0.255 0.333 0.255 0.057

If the coherence values were very low, there was a possibility that the branch building step in the phase unwrapping would fail. Coherence values were not expected to be high in all the data sets because of the quickly changing conditions of the ionosphere, troposphere, and landscape. More information on how the coherence was affected can be found in the results and analysis section.

6.2.4 Phase Unwrapping

Phase unwrapping a SAR image is very intensive and time-consuming. Here the branch-cut region growing algorithm is used because of its robustness and software availability. Because low coherence areas can be problematic by leaving discontinuities in the image, care had to be taken when determining all parameters of the unwrapping stage. First, the image had to be filtered and then residues and neutrons could be determined. Finally, branches could be placed and the image could be unwrapped.

The first step of phase unwrapping is the filtering of the image. Adaptive filtering was used to reduce phase noise and to reduce the number of residues. This low-pass filter would self-adjust to optimize the path of the phase unwrapping branches. Then, the local range slope was computed and the phase in the filtering window was averaged. The size of the filtering window was 4 pixels by 4 pixels and was chosen to prevent too much smoothing and absorb any high or low values that could contribute to noise. Also, to

prevent the inclusion of very low coherence values, a coherence threshold of 0.25 was set.

Another coherence threshold flag was set after the filtering. Any areas below the defined value of 0.1 were flagged and then a 2 pixel border surrounding the low coherence pixel was developed. The border was used to decrease the calculation time by being able to avoid the larger flagged areas faster than having to avoid several single pixels in one small area. In some of the water bodies, shallow vegetation would cause the radar to have a low coherence value and therefore attempt unwrapping, but with a threshold, this effect could be avoided. The stray vegetation pixels within the water bodies would increase calculation time and be ineffective for the purposes of this study. The coherence flags were applied to the filtered image during the following phase unwrapping steps.

The first part of the actual phase unwrapping was to determine the location of the neutrons. Neutrons are defined as areas of the interferogram where the electrical signal is not positive or negative. The intensity of the pixel had to be at least four times the image's average intensity to be a valid neutron location. The neutrons helped reduce the size of the branches and helped reduce the phase unwrapping errors; therefore reducing the calculation time. Next, the residue locations needed to be determined. The residues restrict the branches to stay within a particular path between locations and the "seed" from which the branches were to grow from was set in the center of the image. The maximum branch length was defined as 64 pixels to help prevent straying branches and to increase computation time.

Once the image was completely encompassed by a neutral branch network, the interferogram could be unwrapped. The unwrapping occurred only along the branches and terminated when either the edge of the image was encountered or the branch ended. The unwrapping began at the center of the image, in the same place as the seed and where

the phase was defined as zero. An example of phase unwrapping errors was in the RADARSAT interferogram, where the unwrapped phases appear to be converging to the center of the image (Figure 7.10). One option was to run this step multiple times to reduce the phase unwrapping errors. Unfortunately, because the branch generation was a two to four day process for each interferogram, this was only run once.

The final step in phase unwrapping was connecting the patches of neutral branch networks. This process is called bridging. Phase unwrapping restarted at the end of each bridge and finished with a difference of less than π. Bridging still considered the 2π phase offset that may occur during the processing and adjusted the values accordingly.

6.2.5 Differential SAR Interferometry

For each triplet of images, two interferograms were produced. This allowed for the choice to use either two pass or three pass interferometry for processing. Two pass interferometry was attempted, but because the DEM files were a cause of errors, technique was rejected and three pass interferometry was pursued. The software would repeatedly return to the georeferencing default values and therefore the DEM tiles could not be registered. It was found that three pass differential interferometry was more successful because it did not rely on external data; therefore, it was used in determining the vertical displacement of the topography, with a specific interest in the subsidence of permafrost in the active delta and on the plateau. The topographic (master) interferogram of three pass interferometry is considered to be the DEM of the area while the slave (deformation) interferogram demonstrates the change.

In all the data sets, the June/July pair was used as the topographic pair because of the longer baseline and the limited amount of subsidence that occurs during those months. In

set 3, the topographic pair did not have the longest baseline, which will have amplified the atmospheric delay.

6.2.5.1 ENVISAT ASAR Differential Interferometry

The first step in creating a differential interferogram was to register two unwrapped interferograms, where the slave interferogram's baseline was larger than the master. The baseline difference helped reduce atmospheric noise. Then, the master and slave images were roughly registered by using a quadratic least squares algorithm to adjust for any geometric skew or offset. The same procedure as before was used to register the interferograms.

Once the interferograms had been coregistered, the images were differentially processed. The phase of the slave interferogram was subtracted from the master interferogram using a quadratic linear least squares equation (equation 19). Then using the phase information of the differential interferogram, a metric displacement map was produced. The displacement map in this study can display only one dimension of change because the change in phase is over a single time period. The displacement was first determined in the sensor's look angle direction and then the vertical displacement was calculated. A constant reference height of 0.00 meters was used to enhance any subsidence detected with a precision of one centimeter.

6.2.5.2 RADARSAT Differential Interferometry

The RADARSAT images had to be processed in a different manner from the ASAR images because only one interferogram would unwrap; and therefore the process was slightly more complex. The offsets of the wrapped and unwrapped interferograms were

determined and then a new registering process was introduced. This process was very similar to section 6.2.1, with some small modifications.

The multi-looked intensity images created in section 6.2.1 were used to determine the slant range and azimuth offsets. Again the two-dimensional cross correlation function was used and the peak of the function determined the offsets. This time a patch size of 1024 pixels by 1024 pixels for the correlation function was used.

To determine the sub-pixel accuracy of the co-registration, a cross-correlation optimization was used with a window size of 64 pixels by 128 pixels. Once the precise offsets were determined, a linear least squares polynomial was calculated to provide a global fit of the two interferograms. Any SNR values below the threshold value of 7.0 were rejected in this calculation, therefore eliminating any blunders. Then the interferograms were geometrically transformed using a bilinear registration function.

Finally, the two interferograms were combined to create the differential interferogram. The final image was calculated by the following equation:

$$\phi = (image_1 * factor1 + image_2 * factor2) \bmod 2\pi \qquad [6.3]$$

Where the factors were defined as *factor1* = 1 and *factor2* = -3. These values were chosen from a series of tests where the average signal to noise ratio was found to be the highest. The factors scale the signal noise to help determine the coherence of the final interferogram:

$$\gamma = \frac{\phi_1 \, factor1 + \phi_2 \, factor2}{\sqrt{2}} \qquad [6.4]$$

The reason for dividing by the square root of 2 accounts for the statistical independence of each original interferogram. Leaving the interferograms wrapped increases the sensitivity to differential effects, but reduces the sensitivity to topography once they are combined. The final steps of computing the RADARSAT differential image followed the same process than the ENVISAT ASAR differential interferometry outlined in section 6.2.5.1.

6.2.6 Georeferencing

The images were georeferenced using ESRI ArcGIS 9.2. A Landsat 7 orthophoto of the Reindeer Station area was acquired through GeoBase® and the major water bodies and rivers were digitized. Using the digitized information, the differential interferogram was then georeferenced using relative control points on the rivers and water bodies. The RMSE of the georeferencing was 7.325 meters, approximately one pixel. A RMSE of approximately one pixel is considered suitable because there were no absolute control points within the images and the displacement map had poor resolution of the rivers and water bodies.

6.3 Ground Data

6.3.1 Conventional Leveling

Ground data were acquired during the months of June and August 2005. The four boundary corners and the center of the test site were established using static differential GPS and steel rods. The GPS data were collected in the World Geodetic System (WGS84) for 12 hours per point to reduce multipath effects and to improve the accuracy of the data (Sheng et al., 2007). The internal points used to produce the DEM were

obtained using a Leica 1205 total station and were positioned at approximately 14 meter intervals.

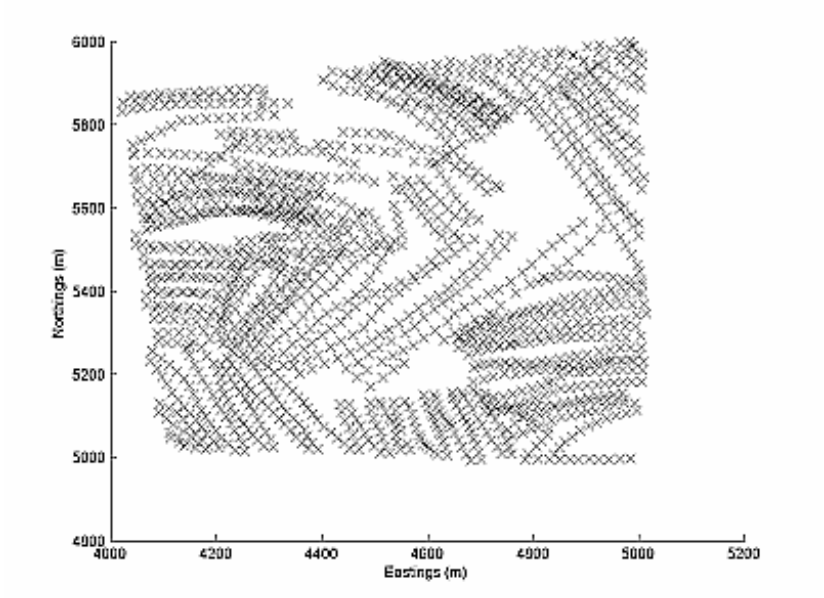

Figure 6.4: June conventional leveling data collection points

The ground data were then processed to create a surface using ordinary kriging and polynomial trend determination using Surfer. As the August data did not work out, the June data was used to create a digital elevation model (DEM) of the area. The DEM was to be used to create a flow accumulation map. A hill shade and aspect map was not considered as an option because of the northern night time sun during the summer, where all aspects receive sunlight throughout the day. A flow accumulation map was hypothesized to have the best qualitative assessment of the spatial structure of the displacement map because the valley floors tend to have a higher accumulation of water; and it is known that as more water stands on a permafrost surface, the more subsidence will occur (Williams & Smith, 1995).

The flow accumulation map was created in ArcGIS 9.2 using the DEM created by the conventional leveling. The georeferenced displacement map was cropped to the area of

interest and the flow accumulation map overlaid. The location and the structure of the flow accumulation lines were analyzed with respect to the higher subsidence areas in the displacement map. If the location and structure of the water accumulation matched the higher subsidence areas, than the displacement map was considered to have acceptable spatial accuracy.

6.3.2 Permafrost Heave Model

To determine the accuracy of the displacement map values, a permafrost heave model created by Gugolj et al. (2008) was used. The permafrost heave model consisted of a thermal regime model (Williams & Smith, 1989; Rankinen et al., 2004), frost front calculations, and heave models (Konrad, 1994; Konrad, 1999). The ground measurements were taken at 36 stations during the summer of 2005 between June 15th and August 27th within the same test site as the conventional leveling, than it was compared to the radar imagery.

6.3.2.1 Thermal Regime Model

The thermal regime model used in creating the permafrost heave model was a simplified version of the finite difference function (Rankinen et al., 2004). The purpose of the model was to calculate the daily ground temperature at one centimeter intervals using a continuous flux. The data required for this model included soil temperature, air temperature, snow depth, and other soil characteristics. The thermal properties of snow were held constant because as fresh snow falls, the wind quickly changes it into a steady state dense snow pack (Williams & Smith, 1989). The peat layer properties were not available so they were considered to be homogenous and therefore were also held constant.

The soil itself was best represented as “silty clay” and the thermal conductivity values taken from Williams & Smith (1989). These values accounted for the variability of thermal conductivity and heat conductivity caused by the mixture of water, ice, and soil. The frost front was also assumed to be at the $0^{o}C$ isotherm (Konrad & Morgenstern, 1981); even though the exact temperature would vary because of geological and chemical variations (Williams & Smith, 1989).

The model would calculate the location of the $0^{o}C$ isotherm within the soil on a daily basis; then it would calculate a linear thermal gradient on either side of the frost front. The algorithm was able to calculate dual frost fronts, as one would ascend from the bottom of the permafrost layer and the other would descend from the surface of the soil.

6.3.2.2 Snow Distribution Model

Understanding the snow distribution is fundamental in predicting the total permafrost coverage in the arctic. Areas with thick, continuous snow coverage tend to have limited amounts of permafrost because snow acts as an insulator. In the test site of this study, the snow was not continuously covering the area. To determine the snow distribution over the test site, a geographic information system (GIS) was used. A DEM of the area was taken and then the daily snowfall, wind magnitude, and wind direction calculated the snow accumulation and distribution on the test site (Gugolj et al., 2008).

6.3.2.3 Heave and Subsidence Model

Other measurements, including the soil moisture and other soil properties, are used to calculate the ice lenses influence on the heave and subsidence of the soil. The heave/subsidence influence in the permafrost heave model is calculated as a direct

relation to the ice lenses' thickness; therefore overestimating the possible subsidence (Konrad, 1999).

The model was run for two years (2004-2005). Figure 6.5 shows the predicted elevation changes in 2005 for the permafrost layer at the station numbered as 54. From the graph, one can see that between June 18th and August 28th, there is a linear subsidence trend. The linear subsidence trend during this period justified using three pass interferometry for DInSAR and that either June/July or the July/August pair could be used as the topographic pair, depending on the length of the baseline.

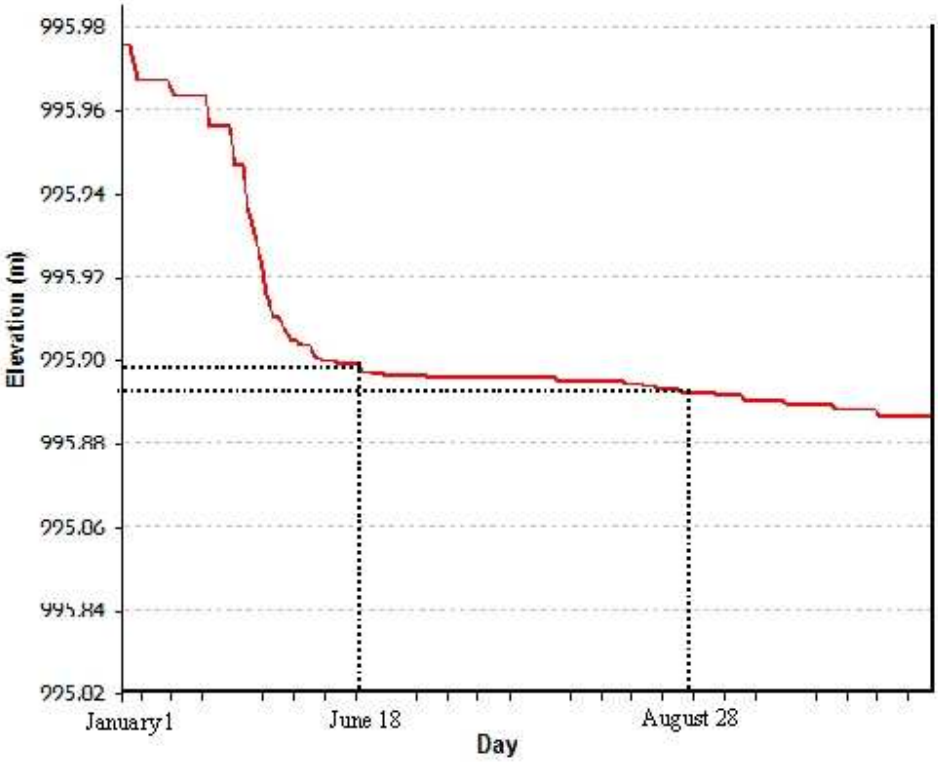

Figure 6.5: Permafrost heave model predicted elevation changes for 2005

(Gugolj, 2006)

CHAPTER SEVEN
RESULTS AND ANALYSIS

7.1 Data Input

The nine ENVISAT images acquired were individually processed by the European Space Agency and the RADARSAT data was created by the Canadian Space Agency. The RADARSAT data had the azimuth data temporally descending throughout the file; therefore, the image had to be flipped to ensure consistency where the earliest azimuth time is at the beginning and the range data runs from near range to far range. Table 7.1 presents the date, orbit, starting time, and size of images and Table 7.2 shows the incidence angle and Doppler polynomial for each image.

Table 7.1: Raw data characteristics of images

Set	Date	Orbit	Starting Time	Size (pixels)	
				Rows	Columns
1	06/18/05	17259	19:32:28	30532	5115
	07/23/05	17760	19:32:28	30519	5115
	08/27/05	18261	19:32:24	30523	5115
2	06/24/05	17337	06:07:21	31873	5099
	07/29/05	17838	06:07:19	31875	5099
	09/02/05	18339	06:07:15	31879	5099
3	06/21/05	17302	19:38:13	27478	6220
	07/26/05	17803	19:38:14	27477	6220
	08/30/05	18304	19:38:09	27482	6220
Radarsat	06/28/05	50365	15:28:59	11702	7695
	08/15/05	51051	15:28:54	11704	7695
	09/08/05	51394	15:28:55	11709	7695

Table 7.2: Incidence angles and Doppler polynomials

Set	Orbit	Incidence Angle (degrees)	Doppler Polynomial
1	17259	37.6053	-153.80147 - 1.63798e-003x - 4.21355e-009x^2
	17760	37.5981	-148.36178 - 1.64303e-003x - 3.38191e-009x^2
	18261	37.6024	-143.64335 - 1.54567e-003x - 4.36597e-009x^2
2	17337	28.6921	-616.19170 - 2.22175e-003x + 2.74605e-008x^2
	17838	28.6803	-623.00048 - 2.28622e-003x + 3.34222e-008x^2
	18339	28.6823	-611.97188 - 2.28630e-003x + 3.62955e-008x^2
3	17302	33.7194	-99.99927 - 2.56401e-003x + 2.54993e-008x^2
	17803	33.7151	-98.42027 - 2.54024e-003x + 2.34796e-008x^2
	18304	33.7181	-92.26037 - 2.41770e-003x + 2.35715e-008x^2
RS	50365	38.5850	4316.11811+8.67323e-003x-3.14452e-009x^2
	51051	38.5870	4200.93817+8.67076e-003x-3.04820e-009x^2
	51394	38.5800	4194.00894+8.52284e-003x-2.73511e-009x^2

It is known that different incidence angles have an effect on the collected backscatter of the radar signal (Ulaby et al., 1986); so therefore, the difference in incidence angles of approximately 10 degrees should present unique results. Set 2 at 28.6^o and Set 3 at 33.7^o are the lowest incidence angles, where the RADARSAT and Set 1 are approximately at 38°.

Also from Table 7.2, one can see that set 2 and RADARSAT (RS) have Doppler polynomials that are much larger than the other sets. The Doppler centroid differences range from 8 dB in Set 3 to 122 dB in RS. The other two sets' Doppler centroid differences are calculated to be 10 dB and 11 dB. The higher value in centroid differences in each of the RADARSAT pairs may cause the coherence and the accuracy to decrease.

7.2 Image Registration

Image registration was very successful for sets 1, 3, and RS. However, there appeared to be problems with registering set 2. The following table shows the calculated precise values of the offsets for each pair in each set:

Table 7.3: Range and Azimuth Offsets of Image Pairs

Set	Pair (by orbit)	Range Offset	Azimuth Offset	Pixel Size (m)	
				Range	Azimuth
1	17760 & 17259	14.400	-53.576	7.8039	15.8894
	17760 & 18261	-24.061	-696.999	7.8039	15.8894
2	17838 & 17337	7.566	-62.499	7.8039	15.7207
	17838 & 18339	-13.277	-0.269	7.8039	15.7207
3	17803 & 17302	6.457	2735.662	7.8039	19.5463
	17803 & 18304	-22.875	1321.189	7.8039	19.5463
RS	0628 & 0815	-37.385	-92.560	4.6382	25.7355
	0815 & 0908	-9.67306	24.87955	4.6382	25.7355

As described in section 6.2.1, a third degree quadratic least squares polynomial was created for each pair. Higher order polynomials were attempted but they were found to decrease the SNR; therefore being a poor representation of the offsets. The following table presents the values of the final SNR for each pair, after all values below 7.0 dB had been removed:

Table 7.4: Signal to Noise Ratio Statistics

Set	Pair (by orbit)	Mean (dB)	Standard Deviation (dB)	Minimum (dB)	Maximum (dB)
1	17760 & 17259	8.9185	1.7108	7.0440	14.7160
	17760 & 18261	8.8258	1.7605	7.0180	17.5280
2	17838 & 17337	8.1934	1.2538	7.0210	12.9270
	17838 & 18339	8.5463	1.6375	7.0160	16.3340
3	17803 & 17302	10.0342	2.2690	7.0010	17.4590
	17803 & 18304	8.6834	1.4824	7.0040	16.3670
RS	0628 & 0815	12.6523	4.4031	7.0080	38.7580
	0815 & 0908	10.3714	2.4469	7.0050	23.6710

The mean SNR value of the ENVISAT images was approximately 9.0 dB. This is not considered a high SNR value, but was considered sufficient for the purposes of this study because the atmospheric activity was neglected. Lower SNR values may affect the coherence and phase unwrapping steps of the processing, where higher SNR values would have been beneficial. Here one can see that RS, set 1, and set 3 have the highest SNR values, where RS was approximately 3 dB higher. Set 2 has slightly lower values (about 0.7 dB lower). From Table 7.2 and Table 7.4, it is expected that Set 3 should be the most successful with having the lowest Doppler Centroid differences and a high SNR value.

7.3 Interferogram Generation

A baseline calculation was required for the interferogram generation and to determine the local incidence angles. Table 7.5 shows the values of each pair's baseline in the range, azimuth, and altitude directions:

Table 7.5: Baselines and their breakdown

Set	Pair (by orbit)	Range (m)	Azimuth (m)	Altitude (m)	Total (m)
1	17760 & 17259	-3.4252383	-324.9551439	66.0883528	-331.6252
	17760 & 18261	3.1731063	299.9314535	36.5106017	302.1622
2	17838 & 17337	-4.3948064	-328.2697054	78.1695971	-337.4771
	17838 & 18339	-4.1558330	241.4206063	12.6431397	241.7872
3	17803 & 17302	0.0002126	-217.2583308	56.3912528	-224.4575
	17803 & 18304	0.0000049	309.0519712	41.5188001	311.8284
RS	0628 & 0815	8.2249127	390.6051381	7.1723845	390.7575
	0815 & 0908	2.5033473	196.4671834	-66.5565341	207.4497

The average baseline is 293.4431 m, which is below the 500 m threshold for satellite pairs in differential interferometry. The largest difference is approximately 183 meters between the RS pair baselines. As the baseline difference increases, the local incidence angle differences will increase; therefore decreasing the coherence. Also, according to Table 7.5, the longest baselines in all sets, except set 3, were found to be in the June / July pair. It was concluded that the June / July pairs would be used as the topographic interferogram (i.e. the slave interferogram) to reduce the atmospheric signal delay.

7.4 Coherence Estimation

Coherence is affected by many factors and this study examines only a few of them. Any change between acquisitions in the surrounding vegetation, water content, air humidity, or ionosphere can reduce the coherence of an image pair dramatically. Because the northern landscape can change abruptly, the coherence of all the pairs was not expected to be high. If the coherence had turned out to be too low, the phase unwrapping step should not be possible.

In Figure 7.1, the images of the resulting Set 1 coherence maps are overlaid on an intensity image. The coherence threshold range was between 0.1 and 0.9. In all subsequent coherence images, there is a linear relationship between the colour value and the coherence value, where black is the lowest coherence and yellow is the highest.

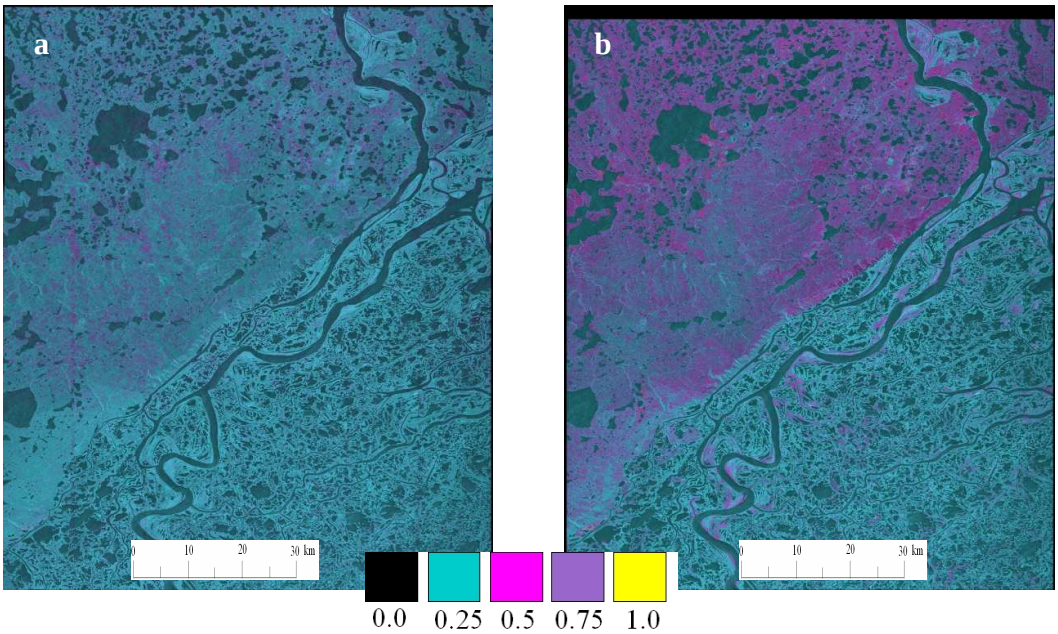

Figure 7.1: a) 17259 & 17760 (June-July) coherence; b) 17760 & 18261 (July-August) coherence

In these images, the dark purple represents a higher coherence than the blue. As expected, the higher coherence was found on the plateau and the active delta has a lower coherence with some small patches of high coherence. This result was not surprising because of the high moisture content and high amount of vegetation in the active delta. Table 7.6 provides the mean, standard deviation, minimum, and maximum for each image in a high coherent area, the test site by Reindeer Station, and a low coherent area (active delta area).

Table 7.6: Coherence Statistics For Set 1

Image	Area	Mean	Standard Deviation	Minimum	Maximum
17760 & 17259	High Coherent area	0.6398	0.2643	0.1	0.8875
	Reindeer Station	0.5681	0.2225	0.1	0.8718
	Active delta	0.5149	0.2510	0.1	0.8655
17760 & 18261	High	0.4694	0.2931	0.1	0.8718
	Reindeer Station	0.4065	0.2073	0.1	0.8341
	Active Delta	0.2443	0.1916	0.1	0.6208

Table 7.6 suggests that the test site by Reindeer Station contains an average coherence compared to the rest of the image. The coherence on the plateau between June and July was higher than between July and August. This difference could mean that there was higher precipitation in August or that vegetation may have changed quickly in August. It also could mean that there was very little deformation during the first epoch. Weather information was not collected in this study, therefore there cannot be any concrete conclusions made if moisture in the troposphere had adversely affect radar signals. The June / July image also shows that Reindeer Station has the lowest standard deviation of coherence and therefore the area was more consistent then the other areas.

Figure 7.2 shows the coherence maps overlaid on the intensity maps for set 2. The scale is the same as with Figure 7.3.

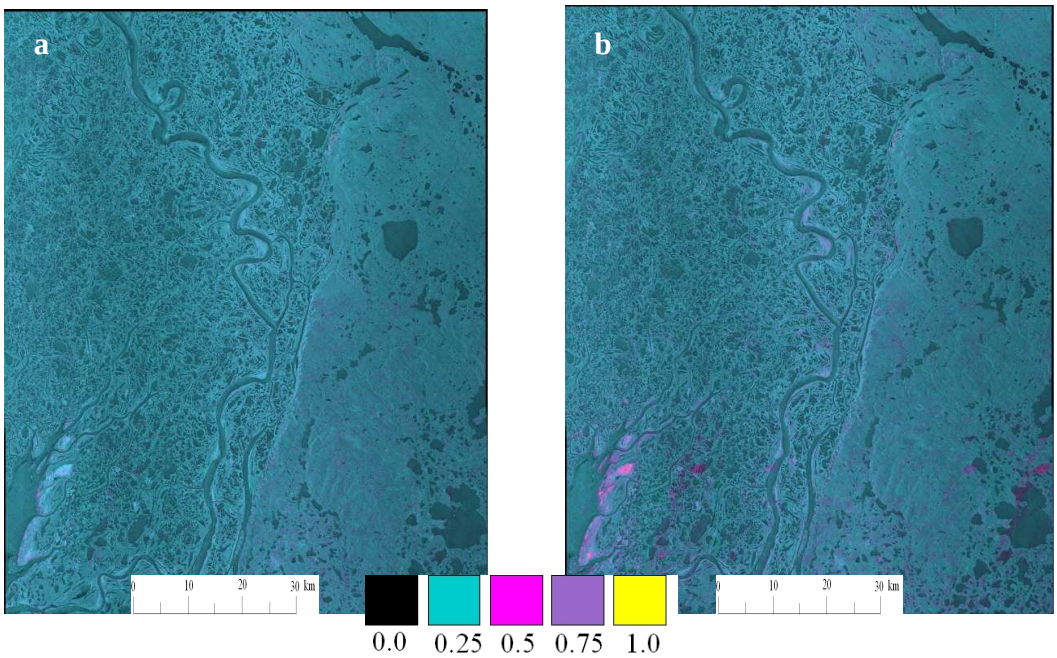

Figure 7.2: a) 17337 & 17838 (June-July) coherence; b) 17838 & 18339 (July-August) coherence

Figure 7.2 shows that set 2 had very low coherence compared to set 1 (Figure 7.1). The high coherent areas in (b) appear to be low in (a). The water bodies also appear to be not as well defined as in set 1 or set 3 (to follow) and the images appear to be mirrored of sets 1 and 3. The poor water body definition illustrates that the lower SNR mean values that were calculated previously may have had an ill effect on the images and because the images are flipped in the registration step, the set 2 mirrored images suggest that the images did not successfully register. It was hypothesized that unwrapping these images may be very difficult. More detail on the unwrapping of these images will follow in section 7.5. The table below shows the mean, standard deviation, minimum, and maximum for this set.

Table 7.7: Coherence Statistics for Set 2

Image	Area	Mean	Standard Deviation	Minimum	Maximum
17337 & 17838	Settlement	0.6438	0.2477	0.1	0.8875
	Reindeer Station	0.5588	0.2212	0.2506	0.8780
	Active Delta	0.5437	0.2416	0.1	0.8655
17337 & 18339	Settlement	0.6843	0.3073	0.1	0.9
	Reindeer Station	0.2882	0.2007	0.1	0.6741
	Active Delta	0.2230	0.1773	0.1	0.6270

Again, one can see difference in mean coherence in August. This difference again may represent faster vegetation growth, more tropospheric moisture, or more subsidence than in June / July.

Set 3's coherence images are presented in Figure 7.3 with the same linear colour-coherence relationship as the previous sets.

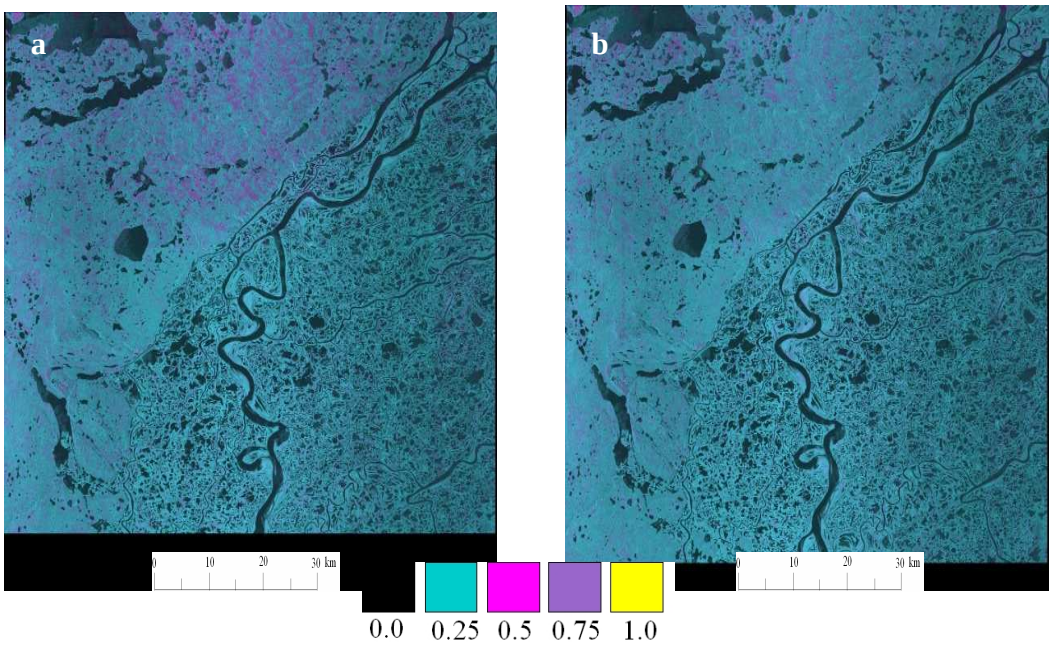

Figure 7.3: a) 17302 & 17803 (June-July) coherence; b) 17803 & 18304 (July-August) coherence

From Figure 7.3, one can see that set 3 has low coherence in the delta with higher coherence patches on the plateau, just as set 1 had shown. The coherence appears to correspond between the two images better than in set 2, so unwrapping this image may be more successful. Table 7.8 will help assist in determining this success.

Table 7.8: Coherence Statistics for Set 3

Image	Area	Mean	Standard Deviation	Minimum	Maximum
17302 & 17803	Settlement	0.6359	0.2565	0.1	0.8875
	Reindeer Station	0.5832	0.2214	0.1	0.8780
	Active Delta	0.4663	0.2264	0.1	0.8623
17803 & 18304	Settlement	0.6281	0.2613	0.1	0.8875
	Reindeer Station	0.5994	0.2216	0.1	0.8718
	Active Delta	0.4876	0.2281	0.1	0.8623

Set 3 had the highest mean coherence values for Reindeer Station. It was concluded that the shorter baselines of set 3 was the contributing factor in increasing the coherence above the one for set 1.

Figure 7.4 presents the resulting coherence maps overlaid on the intensity map for the RADARSAT sets. The threshold range is between 0.1 and 0.9 – same as the ENVISAT images. There is also the same linear relationship between the colour value and the coherence value, where black is the lowest coherence and yellow is the highest.

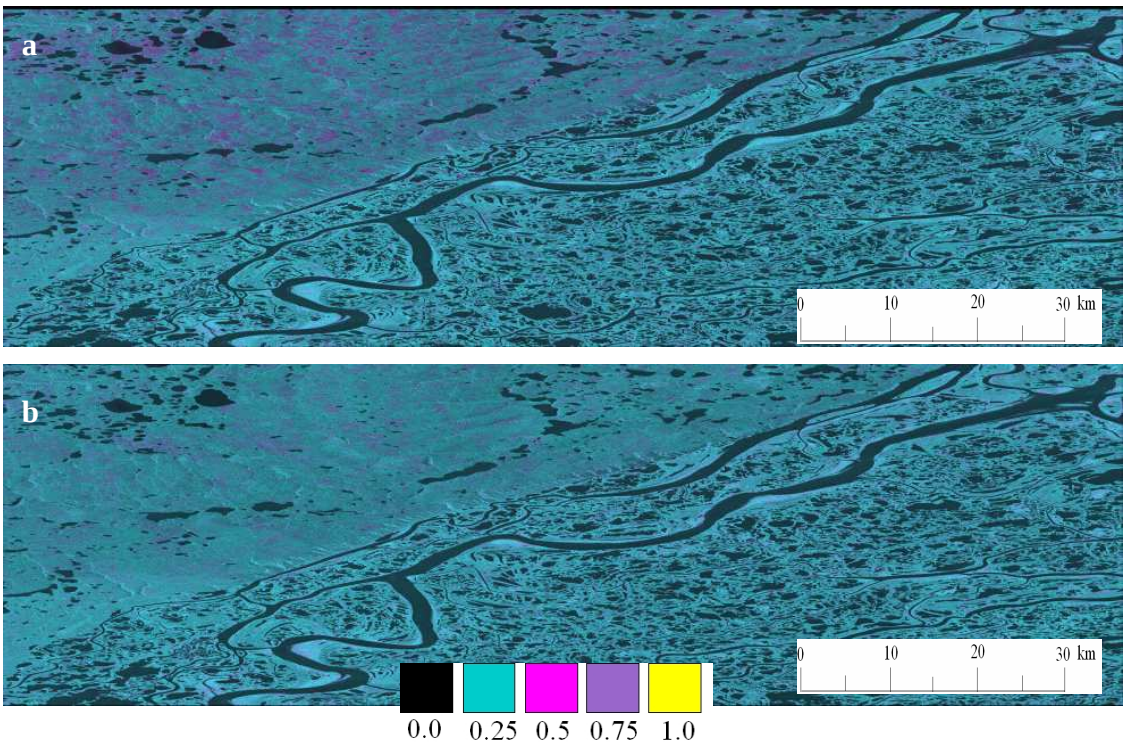

Figure 7.4: a) June / August coherency map; b) August / September coherency map

The RADARSAT coherence estimation appears to be similar to set 3. There are some patches of higher coherence on the plateau in the June-August image (a), where there is lower coherence in the same area in the August-September (b) image. The following table provides the mean, standard deviation, minimum, and maximum for each image in a high coherence area, the test site by Reindeer Station, and a low coherence area (active delta area).

Table 7.9: Coherence Statistics for RADARSAT

Image	Area	Mean	Standard Deviation	Minimum	Maximum
0628 & 0815	Settlement	0.6158	0.2223	0.1	0.8718
	Reindeer Station	0.5476	0.2180	0.1	0.8749
	Active Delta	0.5392	0.2082	0.1	0.8749
0815 & 0908	Settlement	0.6133	0.2190	0.1	0.8718
	Reindeer Station	0.5478	0.2219	0.1	0.8718
	Active Delta	0.4910	0.2827	0.1	0.8780

The mean values for all three areas for both pairs are about 0.5, which is similar to the ENVISAT images. The active delta values are much higher in the RADARSAT pairs than the ENVISAT images.

Set 1 was found to have the most appropriate registration and coherence values of the four sets because of the following reasons. Although the baselines are relatively long, the SNR value was found to be high, the Doppler centroid differences were relatively low, and the coherence values were suitable for proceeding with processing on the plateau. Set 3 also showed the best coherence with the shorter baseline pair. Set 3 also displayed a higher coherence, possibly because its SNR values were higher, the baselines were shorter, and the Doppler centroid differences were lower.

When looking at Figures 7.1 to 7.4, one can see that set 2, set 3, and RADARSAT have more than 50% of the landscape consisting of the active delta; where in set 1, more than 50% of the image consists of the plateau. The active delta contains a large number of water bodies, reducing the areas of possible subsidence detection. These water bodies may contribute to discontinuity of phase unwrapping and lead to unreliable results.

Therefore, although set 3 has the highest mean coherence values by approximately 0.05, the active delta in the image may contribute to erroneous phase unwrapping.

7.5 Phase Unwrapping

Phase unwrapping is the most time-consuming, computationally-extensive process of interferometry. Each interferogram would take up to four days to unwrap. The branch cut algorithm allows the possibility of attempting several possible solutions for creating branches, but because of time restraints, each interferogram was only run with one branch solution.

Unfortunately, at the step of creating the phase unwrapping branches set 2 failed. Not only possibly it failed because of low coherence due to registration failure, it may also have failed because the active delta area was found in the top left hand corner of the image and throughout the center; therefore the phase unwrapping seed was placed in a low coherence area. Several seed locations were attempted, but they had all completed with the same result. Also, because set 2 has the least amount of plateau land, with an average coherence of 0.5007, and had the most active delta area, with an average coherence of 0.2067, the branch solution would have contained a high number of discontinuities and very small branch lengths. A divergence of the number of branches may have caused the algorithm to fail.

Another reason as to why set 2 failed could have been because of high ionospheric activity (Table 7.10). High geomagnetic activity can cause a relative phase shift of a radar signal, therefore reducing coherence between two images (Hanssen, 2001). The nearest station of recorded ionospheric activity was in Yellowknife (Geological Survey of Canada Plotting Service), approximately 1100 km away, and one-minute readings were used for this analysis. Sets 1 and 3 did not have any change in magnetic activity during

any of the acquisitions, but set 2 had a change of 25 nT between June and July and a change of 15 nT between July and August. This change of activity could contribute to the relative phase advancement of one of the radar signals. June and August were attempted to be registered, where only a 10 nT change was detected, but this registration also failed. It was concluded that the main reason for the poor registration results and phase unwrapping failure was a combination of the low incidence angle and the ionospheric activity.

Table 7.10: Ionospheric activity recorded in Yellowknife

Set	Date of Acquisition	Change in mean magnetic activity (nano-Tesla)
1	June / July	0
	July / August	0
2	June / July	-25
	July / August	15
3	June / July	0
	July / August	0
RADARSAT	June / August	-3
	August / September	3

See below for the unwrapped RADARSAT interferograms. These interferograms are coloured depending on differential phase values.

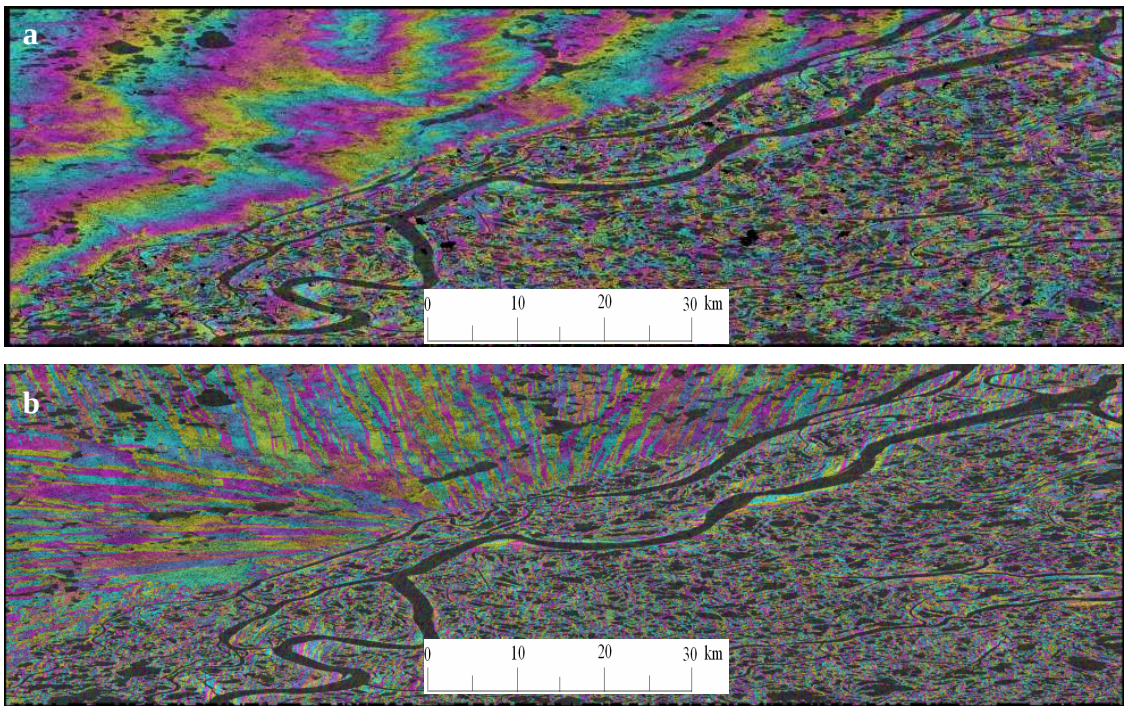

Figure 7.5: a) June / August unwrapped interferogram; b) August / September unwrapped interferogram

When examining Figure 7.5, one can see that there is an apparent problem with unwrapping the RADARSAT images. This was possibly due to the large percentage of active delta in the image or the high Doppler centroid values. When the branches were built, the seeds were place at the center of the image and the results show a convergence to the center, the pattern was not consistent between the two interferograms. The seed was planted at the top left hand corner in one attempt and several other locations in other attempts, but the same systematic error was seen. There appears to be some consistency in the active delta along the levies, but was drastically different the more inland one went to. Cropping the image before unwrapping was also attempted, but gave no results.

7.6 Differential Interferometry

Set 1, set 3, and RADARSAT were used for differential interferometry because their interferograms successfully unwrapped. The first step to create the differential interferogram was to register the two interferograms from the triplet set. In registering the interferograms, there is a pixel offset and a phase offset that is required to be corrected for. After registration, it was found that Set 1 had a 16 pixel offset in both the range and azimuth direction; but there was no need to correct for the phase offset. In other words, the phase offset was zero. Set 3 also had a 16 pixel offset in both the range and azimuth direction, but there was a need to correct for the phase offset. The differential phase fit polynomial for set 3 was the following:

$$\Delta\phi = 21.10822 + 1.0157e\text{-}002x - 3.0660e\text{-}006y - 3.9290e\text{-}001xy$$
$$-1.2528e\text{-}004x^2 + 3.6632e\text{-}003y^2$$

Where *x* and *y* are the phase values in the range and azimuth directions. An unwrapped differential interferogram was developed by determining the phase differences between the slave interferogram and the master interferogram. Figure 7.6 presents the unwrapped differential interferogram for set 1 (a) and for set 3 (b).

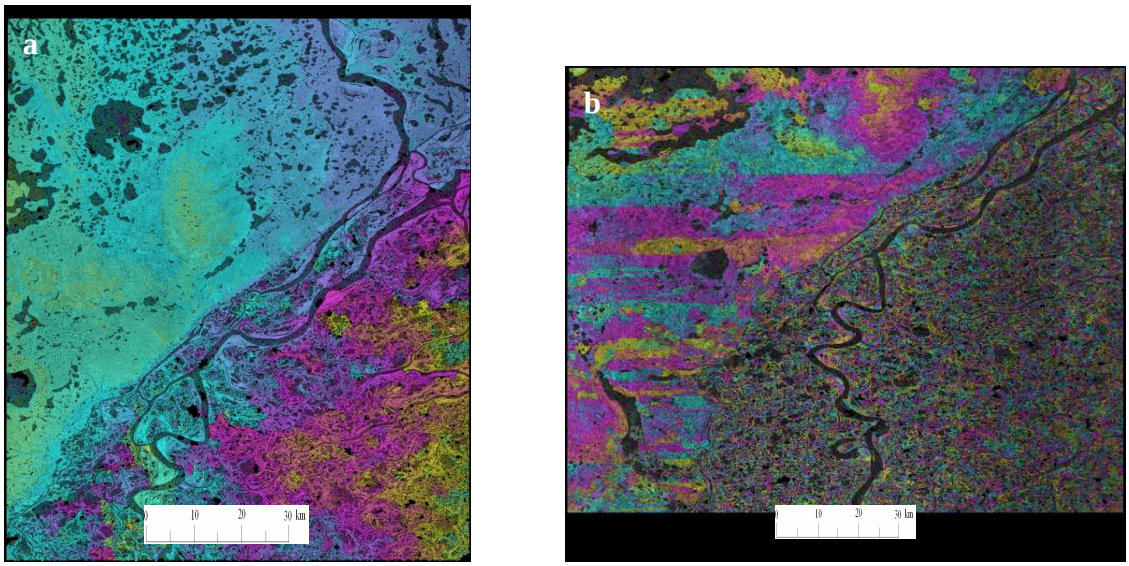

Figure 7.6: a) Set 1 unwrapped differential interferogram; b) Set 3 unwrapped differential interferogram

In both images, one can see that there is disarray in the active delta. Although, in set 1 (Figure 7.6a), there are rings around the water bodies which represent the levies. The rest of the data in the delta does not show a natural pattern of phase information, but shows a gradual phase change towards the right (or East). A natural pattern would show pockets of subsidence around the water bodies. The reason as to why the delta shows very little information may be due by the high number of water bodies that caused discontinuities along the branches in the phase unwrapping stage and therefore did not provide reliable differential results. On the plateau, there are some gradual transforming yellow areas that represent pockets of subsidence. A colour map to enhance the yellow areas was used and the image was cropped to one of the pockets (Figure 7.7). In Figure 7.7, one can clearly see the pocket of phase differences on the plateau and the phase changes along the levies.

In Figure 7.6b, set 3 did not appear to have a natural trend. It appeared that there could be some significant subsidence, but the horizontal striping pattern of the phase difference does not appear to contain natural pockets. Patterns similar to this could be caused by

atmospheric delay. As mentioned previously, a shorter baseline pair was used as the topographic pair, which can amplify the atmospheric delay. The striping pattern could be caused by local ionospheric or tropospheric effects. But because the ionospheric data was not obtained for the test site and the tropospheric effects were not measured, this could not be concluded. Also, in the active delta, one can see the levies again along the river and water bodies, but even more disarray appears in the area. It was decided to attempt the displacement map to see if a natural subsidence pattern would result.

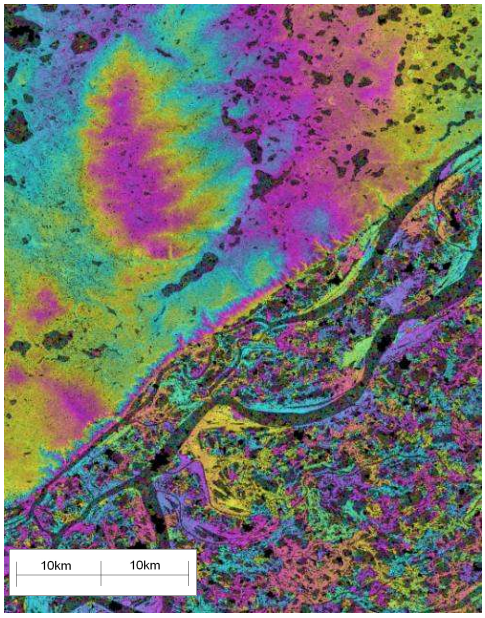

Figure 7.7: Enhanced image of set 1 differential interferogram

Figure 7.8 show set 1 and set 3's displacement maps.

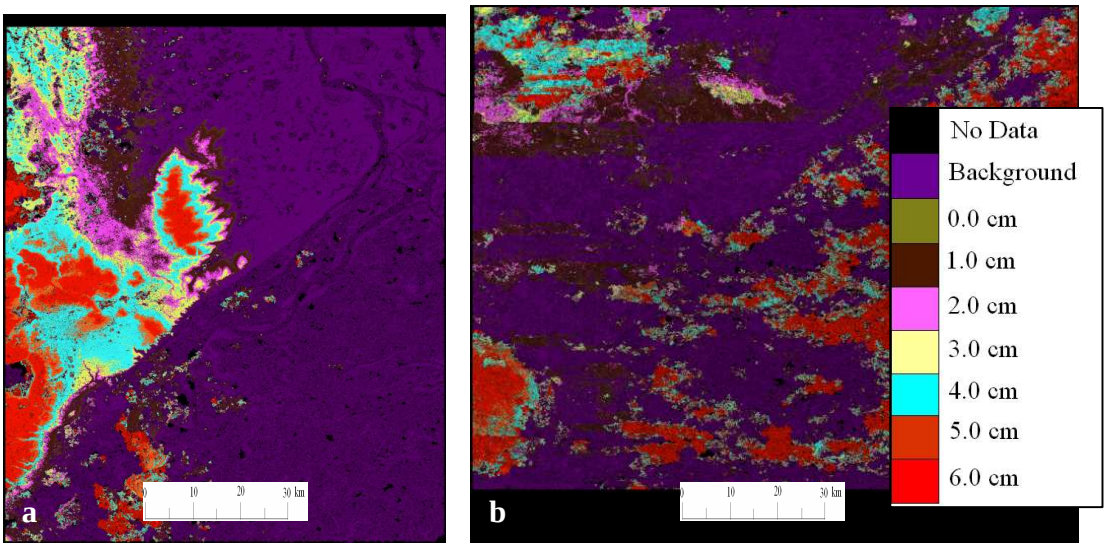

Figure 7.8: a) Set 1 displacement map; b) Set 3 displacement map

The displacement maps were created with a colour map using the single hexagon value index at 1 cm intervals. Positive values indicate subsidence, while negative values indicate some upheaval. Figure 7.9 is an example of the colour map file used. The columns of the colour map were (from left to right) vertical displacement, hue, saturation, and intensity. *B* stands for background areas and *F* stands for forefront areas. These areas consist of the areas that failed to unwrap. As mentioned previously, the topography needs to be removed to create a reliable differential interferogram. It is believed that the topography has been correctly removed from the interferograms because the subsidence pattern on the plateau is not defined by topographic formations, such as the rolling hills. The subsidence appears to end at the delta because of the number of water bodies and poor phase unwrapping in that area; it is not caused by the topographic effect.

```
# Colour map for DInSAR displacement map

          -0.13   300     0.95    0.85
          -0.12   285     0.90    0.90
          -0.11   270     0.85    0.90
           -0.1   255     0.80    0.90
          -0.09   240     0.75    0.90
          -0.08   225     0.70    0.95
          -0.07   210     0.65    0.95
          -0.06   195     0.60    0.95
         -0.05   180      0.55    0.95
         -0.04   165      0.50    0.95
         -0.03   150      0.95    0.95
         -0.02   105      0.40    0.95
        -0.01    50       0.35    0.85
           0       0     0.30    0.70
         0.01     300     0.95    0.70
          0.02     65     0.95    0.70
        0.03     180      0.95    0.80
         0.04    120      0.95    0.80
          0.05    20      0.95    0.90
            0.06    5      0.95    1
           B       290     0.45    1.0
           F       0       1.00    1.0
```

Figure 7.9: Colour map used to visualize displacement

Figure 7.8a had the most promising results compared to Figure 7.8b. The differential interferogram of set 3 did not show an appropriate displacement map with natural subsidence pockets. In set 1, one could still see the Caribou Hills and some outlines of the major rivers, where set 3 had lost all topographic qualities. The differential interferogram represented the same pattern found with atmospheric delay amplification. After a close examination of the baselines, it was found that the topographic pair had the shortest baseline, instead of the longest. As mentioned in section 3.2.1, the topographic pair needs to have the longest baseline otherwise the atmospheric delay will be amplified. At this point, set 3 was not used for any further analysis.

The Radarsat differential interferometry had to be completed in a different way from the ENVISAT images because of the obvious systematic errors in the phase unwrapping. The first step was to compute the offsets of the pairs. The offset was found to be zero

using a 64 pixel by 128 pixel estimation window, but a phase fitting model was required. The phase fitting polynomial was found to be:

$$\Delta\phi = -90.33059 + 3.9302e-002x - 1.3879e-006y + 8.9966e-001xy - 2.8762e-004x^2 - 1.2169e-003y^2$$

The size of the estimation window allowed for the SNR to increase. The threshold of 7.0 dB was still used, therefore producing the following statistics:

Table 7.11: RADARSAT Signal to Noise Ratio Statistics

Mean (dB)	Standard Deviation (dB)	Minimum (dB)	Maximum (dB)
38.4862	22.9760	7.0830	91.3290

A phase shift of approximately 90 degrees also helped enhance the SNR values. The mean value was almost four times higher than in the original image registration, although because of the large range of values, the standard deviation was much higher. The next step of this process was to resample one interferogram as the slave to the master interferogram. Then finally, the two wrapped interferograms were combined to produce a wrapped differential interferogram (Figure 7.10) and the baselines between each pair were determined (Table 7.12).

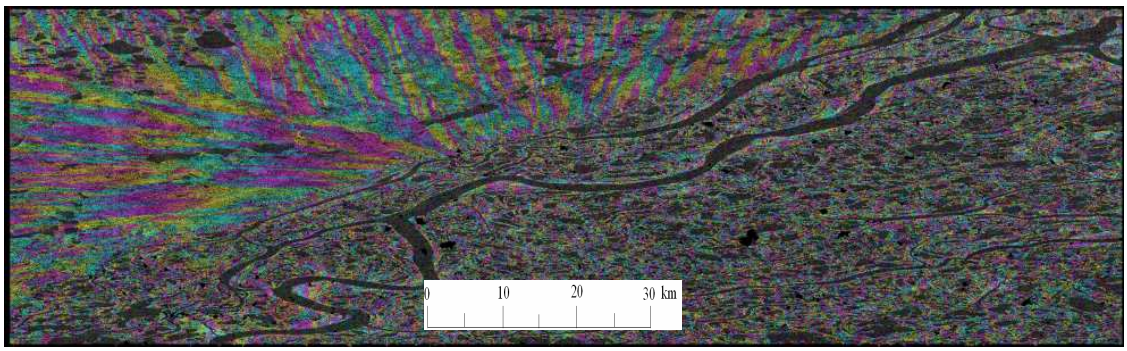

Figure 7.10: Unwrapped RADARSAT differential interferogram

Table 7.12: RADARSAT Baseline

Range (m)	Azimuth (m)	Altitude (m)	Total (m)
-15.7349546	-198.7964121	206.8419868	287.3173

The baseline was relatively small between the two interferograms at 287 meters, but the phase unwrapping appeared to inherit the same pattern as the unwrapped interferogram in Figure 7.5b. This result may have occurred because of the high percentage of the active delta in the area or because of the high Doppler centroid values. A displacement map was created to see if a result could be recovered from the apparent error (Figure 7.11).

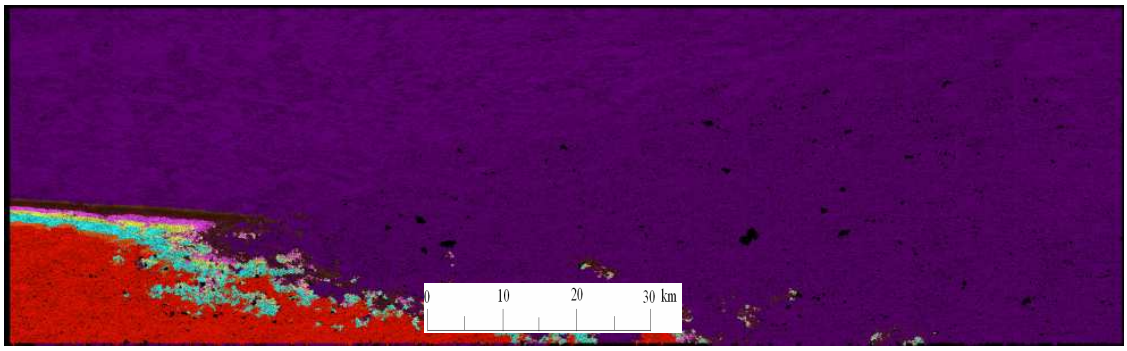

Figure 7.11: RADARSAT displacement map

The displacement map was created using the same colour map as the ENVISAT images. The image unfortunately did not produce any results that could be corroborated with the ground data. The displacement did not seem to correspond to any particular land mass and only appeared at the south end of the image. It also did not follow the similar pattern than the other two sets that used unwrapped interferograms. The possible reason for this result could be attributed to the high Doppler centroid differences found in the pair of interferograms or atmospheric effects. Therefore, the RADARSAT images were not analyzed any further, but were used as an example of high Doppler centroid differences.

To enhance the displacement of set 1, a new colour map was used and then the image was georeferenced (Figure 7.12). There was subsidence of up to 6 cm found on the plateau, but areas of missing information could also be seen. These areas include the delta and the northern part of the plateau. It was concluded that the reason behind the missing information was because of the higher number of present water bodies causing phase unwrapping discontinuities. The new subsidence map was then cropped down to the test site by Reindeer Station (Figure 7.12) so a comparison could be completed.

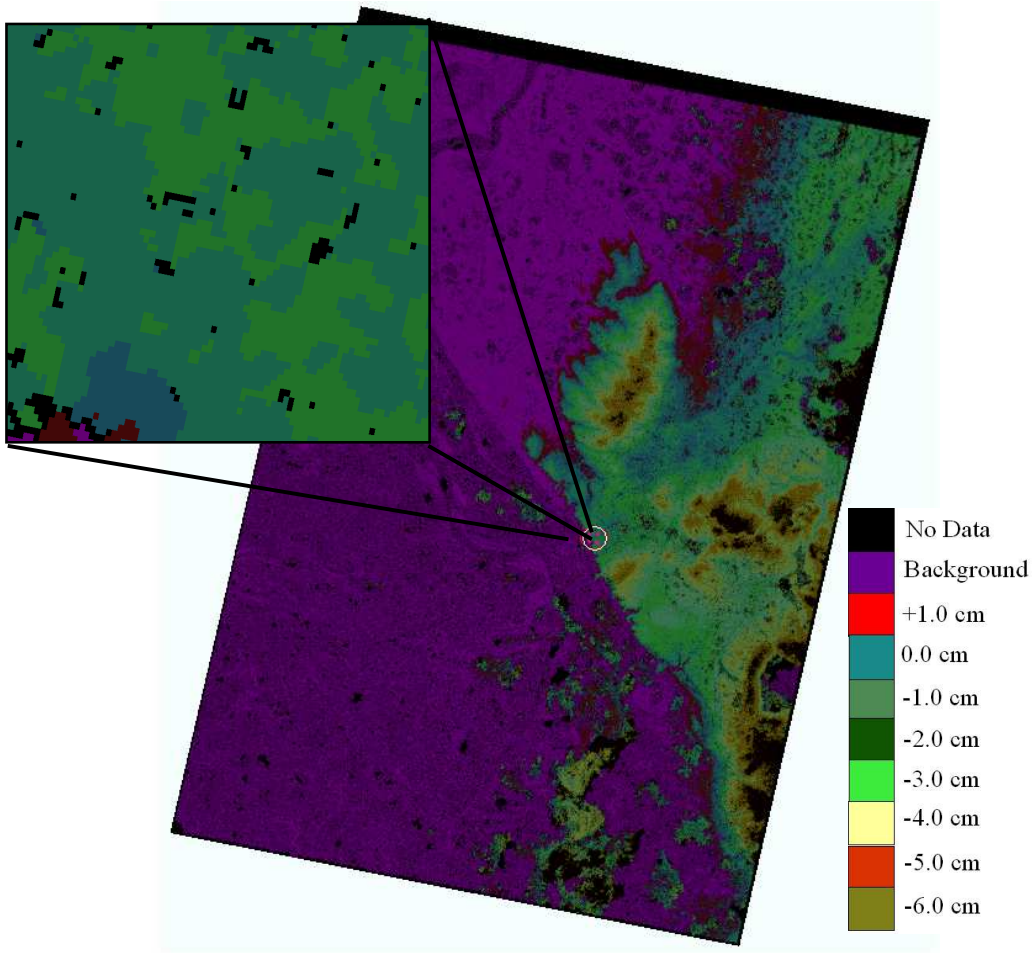

Figure 7.12: Displacement map of set 1 where blue shows zero subsidence and brown shows 6 cm of subsidence and an enlargement of the area of interest

7.7 Ground Data Correlation

As mentioned in section 6.3.1, an attempt was made to compare the land structure of the test site using a flow accumulation map. Figure 7.13 shows the flow accumulation map (the bright red lines) laid over the interferogram of the test site. It was impressive to see how well the accumulation map corresponded with the interferogram. Similar structures in both maps, such as the U shape area near the center of the image, were found to relate

very well. It was apparent that there was a differential scale problem, but the relationship was high enough to show that the results were not coincidental.

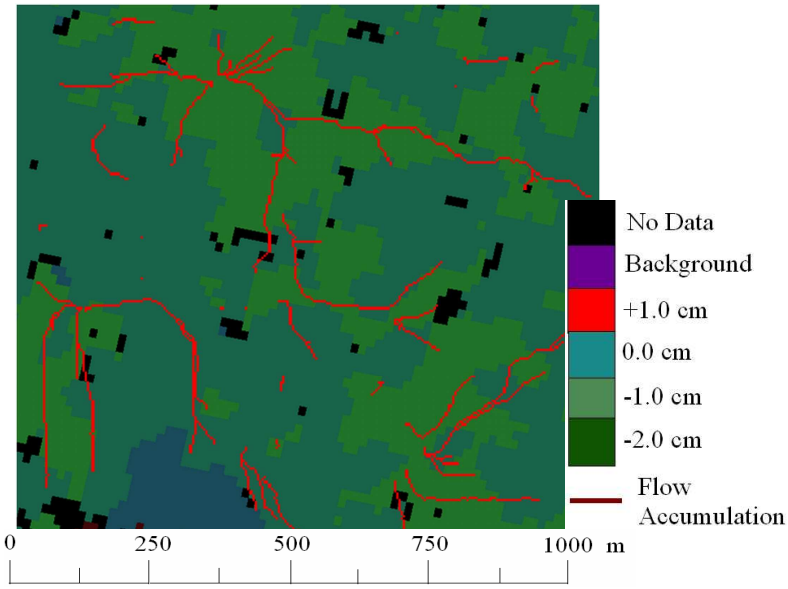

Figure 7.13: Differential interferogram of the area of interest with flow accumulation map overlaid

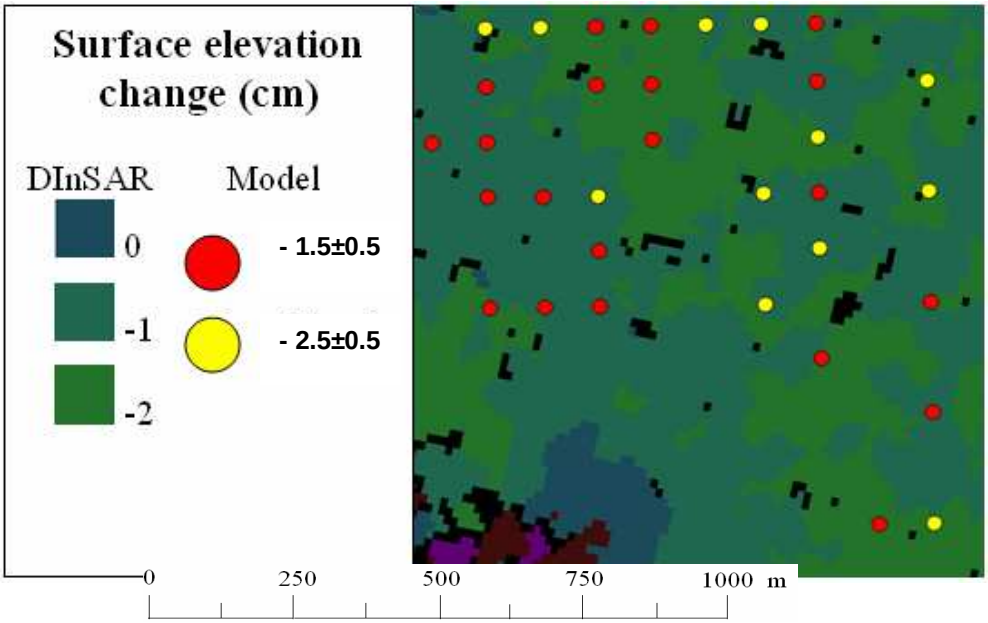

Figure 7.14: Displacement map compared with the permafrost heave model

Because the flow accumulation map of the DEM attested to the structural composition of the interferogram, the next important comparison was to ensure that the magnitude of the interferogram was also correct. Subsidence of up to 2 cm can be seen in Figure 7.14, where the permafrost heave model shows a subsidence of up to 3 cm, with an average of 1.9 cm +- 1.5 cm, during the months of June through August. The correlation of the magnitude was also remarkable in this case. The differences in magnitude could be attributed to the fact that DInSAR averaged the scattering response over a large area (7 m by 15 m), where the heave model was a discrete point.

CHAPTER EIGHT
CONCLUSIONS AND RECOMMENDATIONS

8.1 Conclusions

This study is a preliminary study of the use of DInSAR in monitoring permafrost subsidence. Promising results have been found in one of the four sets and therefore additional work and research is still required to develop more concrete conclusions.

From the analysis of Set 1, it was found that there was an intraseasonal subsidence up to 6 cm on the plateau and 3 cm subsidence in the area of interest between June 18th and August 27th, which appears reasonable when compared to the permafrost heave model. There was a lack of information in the active delta and in the northwest section of the image. This deficiency was possibly created by the problems with the branch cut phase unwrapping algorithm.

Four displacement maps were created with centimeter accuracy. After processing and analyzing these image sets, it became apparent that ENVISAT set 1 was the only data set that appeared to process correctly. Set 1 was found to have shorter baselines, a higher SNR, similar Doppler centroid differences, and similar ionospheric activity values than Set 3. The possible reason for the result differences is that Set 1 had the higher incidence angle and that the baseline correction may have caused an amplified atmospheric effect. Set 2 had unsuccessful geometric registration and the reason for this was thought to be from the lowest incidence angle and higher ionospheric activity. RADARSAT had the shortest baseline and the highest SNR, but was found to provide incorrect results. It is believed that the poor results were because of the large Doppler centroid change (122dB) in one of the pairs.

The most prominent factor that appeared to affect the results was the phase unwrapping algorithm. It appears that the branch cut algorithm had difficulties unwrapping the images because of the number of water bodies and the relatively low coherence. When creating the branch network, the algorithm appears to have a diverging number of branches, causing it to crash or provide poor results.

From the other image sets that did not process correctly, it could be concluded that possibly the extent of high coherence areas in an image greatly affects the ability to provide results. The number of discontinuities in the phase cycles greatly increases when there is a high number of water bodies.

As Ulaby et al. had reported in 1986, the incidence angle also had an effect on the processed image quality. Set 1 had an incidence angle of 37.5 degrees and was the only data set that works properly. The optimal incidence angle in the arctic on plateau land may be around 37 degrees as RADARSAT did not work at 38.5 degrees and set 3 did not work at 33.7 degrees.

The environmental, atmospheric, tropospheric, and ionospheric changes could have also affected the radar signal and therefore providing biased results. As in Set 2, the geomagnetic differences at the time of capture in the ionosphere were found to be the highest and it was the first image to show poor results. Environmental, atmospheric, and tropospheric changes were not taken into account. These changes may have also affected the sets and may have attributed to a possible bias of the results of Set 1 and therefore creating inaccurate values. Another factor that appeared to affect the images was the Doppler centroid differences. The data sets with the high Doppler polynomial values also processed incorrectly.

Finding enough similar images to create a high redundancy of data was found to be very difficult in this line of work. Environmental changes happen quickly and with the local incidence angle changes, Doppler centroid differences, and atmospheric effects, it can be difficult to determine one factor affecting the results of the radar signal. Isolating each independent variable requires more data than just four sets of images.

At the conclusion of this study, only one displacement was successfully created. This map may not be completely accurate as there were several factors that were not taken into consideration – such as the tropospheric and local ionospheric data – but it was found that the results did correspond well with ground data.

Relating the interferogram with the aspect map of digital elevation model created by conventional surveying was attempted but was found to be inaccurate. The inaccuracy was caused by the 24 hour sun the area has during the summer; therefore the aspects covered a 360° circle. But when a flow accumulation map was created with the same model, a good correspondence was found with the valley floors and higher areas of subsidence.

A correspondence was found between the interferogram and the permafrost heave model. The heave model used point data locations within the area of interest and these points corresponded very well with the interferogram. The differences seen are possibly because the information found in the pixels in the interferogram is averaged over a large area while the permafrost heave model is point data.

In conclusion, a deformation map was created for an area of 1500 km2 on plateau land and the same processing method could be used for other plateaus that consist of 7% of the northern landscape. It was found that the incidence angle, Doppler centroid differences, and phase unwrapping algorithms may be the cause of error in completing this work.

Because of the lack of redundancy, no results can be guaranteed. With additional work and research, DInSAR could be used to monitor annual changes and monitor the effect of climate change on permafrost in a more cost effective manner.

8.2 Recommendations

This project still requires more research, processing, and ground work to be more conclusive. The following points are suggestions for future research.

- More research into the number of triplets required should be completed. Redundancy is difficult to obtain in the arctic because of the effects of geometric and environmental parameters and their numerous possibilities.

- The effect of the incidence angle on DInSAR in this area should be further researched. Previously, Bamler & Hartl (1998) had recommended an incidence angle of 45° for DInSAR, but in this study the highest incidence angle was 38°. More images should be acquired with different incidence angles to determine the optimal angle.

- Several factors can affect the quality of the results and three of these factors were not accounted for – environmental, tropospheric, and ionospheric. A scatterometer could be used to help determine dielectric constants of the changing surface vegetation and perhaps develop a new way to increase coherence. To account for ionospheric and tropospheric effects, differential global positioning systems could be used to gather the information and then implemented in the processing of the radar images.

- Doppler centroid differences also played an important role in affecting the interferogram results. These differences should also be tested in the future to determine if the Doppler values truly affect differential interferometry results in northern environments.

- Timing of the acquisitions is also important. For example, when the snow first disappears off the surface, it is predicted by the permafrost heave model that the greatest amount of subsidence occurs. When gathering the radar images, it would be important to acquire more imagery around this time so a more accurate conclusion of yearly subsidence can be made.

REFERENCES

Abdelfattah, R. and Nicola, J. 2003. InSAR Coherence Optimisation using Second Kind Statistics, *IGARSS* **6**: 3799-3801.

Allard, M., and Rousseau, L. 1999. The internal structure of a palsa and a peat plateau in the rivie`re Boniface region, Que´bec: Inferences on the formation of ice segregation mounds, *Geogr. Phys. Quat.* **53**: 373–387.

Anderson, C. 1995. Fringe visibility, irradiance, and accuracy in common path interferometers for visualization of phase disturbances, *Applied Optics* **34(32)**: 7474-7485.

Anisimov, O. and Belolutskaya, M. 2002. Evaluation of the effect of climate change and permafrost degradation on infrastructure in the northern regions of Russia, *Russian Meteorology and Hydrology* **6**: 9-14.

Anisimov, O. and Poliakov, V. 2003. GIS assessment of climate-change impacts in permafrost regions, *8th International Conference on Permafrost*, Balkema: Zurich; 9–14.

Annan, A. and Davis, J. 1978. High frequency electrical methods in the detection of the freeze–thaw interface, *Third International Conference on Permafrost* **1:** 495–500.

Bamler, R. 1992. A comparison of range-Doppler and wave number domain SAR focusing algorithms, *IEEE Transactions of Geoscience and Remote Sensing* **30(4)**: 706-713.

Bamler, R. and Hartl, P. 1998. Synthetic aperture radar interferometry, *Inverse Problems* **14(4)**: R1-R54.

Bamler, R. and Just, D. 1993. Phase statistics and decorrelation in SAR interferograms, *IGARSS* **3:** 985-987.

Barsch, D. 1993. Periglacial geomorphology in the 21st century, *Geomorphology* **7**: 141–163.

Beltrami, H. and Taylor, A. 1994. Records of climatic change in the Canadian Arctic: combination of geothermal and oxygen isotope data yields high resolution ground temperature histories. *EOS, Transactions, American Geophysical Union* **57(44)**: 75.

Billings, W. 1987. Constraints to plant growth, reproduction, and establishment in Arctic environments, *Arctic & Alpine Research* **19(4)**: 357-365.

Bracewell, R. 1986. *The Fourier transform and its applications*, McGraw-Hill, New York. 3rd edn.

Brown, J., Hinkel, K.M., and Nelson, F.E. 2000. The Circumpolar Active Layer Monitoring (CALM) Program: Research Designs and Initial Results, *Polar Geography* **24(3)**: 165-258.

Burgess, M., Smith, S.L., Brown, J., Romanovsky, V., Hinkel, K. 2000. Global Terrestrial Network for Permafrost (GTN-P): permafrost monitoring contributing to global climate observations. *Geological Survey of Canada*, 1 –8 (Current Research 2000-E14).

Butterworth, C. and Tait, M. 2007. Monitoring Permafrost Deformation, *Proc. International Circumpolar Conference on Geospatial Sciences and Applications* (CD).

CALM Site Homepage. 2006. Available at: http://www.udel.edu/Geography/calm/

Canadian Geographic. 2008. The Far North: Arctic and Taiga. *The Canadian Atlas Online*, Available at: http://www.canadiangeographic.ca/atlas/themes.aspx?id=artic &lang=En

Carnec, C. and Delacourt, C. 2000. Three years of mining subsidence monitored by SAR interferometry, near Gardanne, France**,** *Journal of Applied Geophysics* **43(1)**: 43-54.

Couture, R., Smith, S., Robinson, S., Burgess, M., and Solomon, S. 2003. On the hazards to infrastructure in the Canadian North associated with thawing of permafrost, *Geohazards 2003, 3rd Canadian Conference on Geotechnique and Natural Hazards*. The Canadian Geotechnical Society: Edmonton, Alberta, Canada; 97–104.

Cramer, M., Ferland, R., and Snay, R. 1999. Realization and unification of NAD83 in Canada and the U.S. via the ITRF, *International Symposium of the International Association of Geodesy* **2**, Munich, October 5-9.

Crippa, B., Crosetta, M., Biescas, E., Troise, C., Pinque, R., and De Natale, G. 2006. An advanced slip model for the Umbria-Marche earthquake sequence: coseismic displacements observed by SAR interferometry and model inversion, *Geophys. J. Int.* **164 (1)**: 36–45.

Cumming, I. and Wong, F. 2005. *Digital processing of Synthetic Aperture Radar Data – Algorithms and Implementation*. Artech House, Inc., Norwood, MA.

Cusack, R., Huntley, J., and Goldrein, H. 1995 Improved noise immune phase unwrapping algorithm, *Applied Optics* **35,** 781–789.

Davis, T. 2001. *Permafrost: a Guide to Frozen Ground in Transition*. University of Alaska Press: Fairbanks.

Denbigh, P. 1995. *System Analysis and Signal Processing with Emphasis on the Use of Matlab*, Addison-Wesley, Boston, MA.

Dionne, J. 1978. Formes et phe´nome`nes pe´riglaciaires en Jame´sie, Que´bec subarctique, *Geogr. Phys. Quat.* **32**: 187– 247.

Doolittle, J., Hardisky, M., and Gross, M. 1990. A ground penetrating radar study of active layer thicknesses in areas of moist sedge and wet sedge tundra near Bethel, Alaska,U.S.A. *Arctic and Alpine Research* **22**: 175–182.

Doolittle, J., Hardisky, M., and Black, S. 1992. A ground penetrating radar study of Goodream Palsen, Newfoundland, Canada, *Arctic and Alpine Research* **24**: 173–178.

Eldhuset, K., Andersen, P., Hauge, S., Isaksson, E. and Waydahl, D. 2003. ERS tandem InSAR processing for DEM generation, glacier motion estimation and coherence analysis on Svalbard, *Int. J. Remote Sens.* **24(7):** 1415-1437.

European Space Agency. 2006. ASAR Products and Algorithms. Available online at: http://envisat.esa.int/dataproducts/asar/CNTR2-6.htm

Fialko, Y., Sandwell, D., Simons, M., and Rosen, P. 2005. Three dimensional deformation caused by the Bam, Iran, earthquake and the origin of shallow slip deficit, *Nature* **435,** 295-299.

Fielding, K. and Dupre, E. 1999. RNGCHN: A program to calculate displacement components from dislocations in an elastic half-space with applications for modeling geodetic measurements of crustal deformation, *Geophysical Research Letters* **25:** 695 – 704.

Flato, G., Boer, G., Lee, W., McFarlane, N., Ramsden, D., Reader, M., and Weaver, A. 2000. The Canadian Centre for Modelling and Analysis Global Coupled Model and its climate, *Climate Dynamics* **16**: 451–467.

Foody, G. and Curran, P. 1994. Environmental Remote Sensing from Regional to Global Scales, *John Wiley & Sons*, Chichester, England, pp. 8-10, 202-207.

French, H. 1996. *The Periglacial Environment*. Addison Wesley Longman: London, UK.

Gabriel, A., Goldstein, R., and Zebker, H. 1989. Mapping small elevation changes over large areas: differential radar interferometry, *Journal of Geophysical Research* **94(B7)**: 9183 – 9191.

Ghiglia, D. and Pritt, M. 1998. *Two Dimensional Phase Unwrapping: Theory, Algorithms, and Software*. John Wiley & Sons Inc.

Goldstein, R. 1995. Atmospheric limitations to repeat-track radar interferometry, *J. Geophys. Res.* **22:** 2517–2520.

Goldstein R. and Zebker, H. 1987. Interferometric radar measurement of ocean surface currents, *Nature* **328(6132)**: 707-709.

Goldstein, R., Zebker, H., and Werner, C. 1988. Satellite radar interferometry: two dimensional phase unwrapping, *Radio Sci.* **23,** 713–720.

Graham, L. 1974. Synthetic interferometer radar for topographic mapping, *Proc. IEEE* **62(6):** 763-768.

Granberg, H. 1994. Mapping heat loss zones for permafrost prediction at the northern/alpine limit of the Boreal forest using high-resolution C-Band SAR, *Remote Sens. Environ.* **50(3)**, 280-286.

Gray, A., Mattar, K., and Sofko, G. 2000. Influence of Ionospheric Electron Density Fluctuations on Satellite Radar Interferometry, *Geophysical Research letters* **27(10):** 1451-1454.

Gruza, G. and Rankova, E. 1980. *Structure and Variability of the Observed Climate. Air Temperature in the Northern Hemisphere*. Gidrometeoizdat, Leningrad.

Guglielmin, M. 2006. Ground Surface Temperature (GST), Active Layer and Permafrost Monitoring in Continental Antarctica, *Permafrost and Periglac. Process.* **17**: 133–143.

Guglielmin, M. and Dramis, F. 1999. Permafrost as a climatic indicator in northern Victoria Land, Antarctica, *Annals of Glaciology* **29:** 131–135.

Gugolj, D. 2006. *Permafrost Active Layer Motion Modeling: A Geographic Information Systems (GIS) Approach*, MGIS Project, Department of Geography, University of Calgary.

Gugolj, D., Moorman, B., and Tait, M. 2008. Development and Initial Evaluation of a Daily DEM-Based Active Layer Heave and Subsidence Model, *Ninth International Conference on Permafrost*, June 29 – July 3.

Gutmann, B. and Weber, H. 2000. Phase unwrapping with the branch-cut method: role of phase-field direction, *Applied Optics* **39(26)**: 4802-4816.

Haeberli, W., Cheng Guodong, Gorbunov, A., and Harris, S. 1993. Mountain Permafrost and Climate Change, *Permafrost and Periglacial Processes* **4(2)**: 165 – 174.

Hall-Atkinson, C. and Smith, L. 2001. Delineation of delta ecozones using interferometric SAR phase coherence Mackenzie River Delta, N.W.T., Canada, *Remote Sens. Environ.* **78**: 229– 238.

Hanssen, R. 2001. *Radar Interferometry: Data Interpretation and Error Analysis*. Kluwer Academic Publishers.

Hanssen, R. 2006. Temporal Decorrelation. Available online: http://earth.esa.int/workshops/ers97/papers/hanssen/node7.html

Hanssen, R. and Feigt, A. 1996. A first quantitative evaluation of atmospheric effects on SAR interferometry, *FRINGE 96' workshop on ERS SAR Interferometry* **ESA SP – 406:** 277 - 282.

Harris, C., Vonder Mühll, D., Isaksen, K., Haeberli, W., Sollid, J., King, L., Holmlund, P., Dramis, F., Guglielmin, M., and Palacios, D. 2003. Warming permafrost in European mountains, *Global and Planetary Change* **39**: 215–225.

Hauck, C. and Vonder Mühll, D. 2003. Evaluation of geophysical techniques for application in mountain permafrost studies, *Geophysical methods in geomorphology* **132**: 161–190.

Heginbottom, J. 1973. Some effects of surface disturbance on the permafrost active layer at Inuvik, N.W.T., Canada, *2nd International Permafrost Conference* **North American Contribution**: 649-657.

Hein, A. 2004. *Processing of SAR Data*. Springer, New York.

Hinkel, K., Paetzold, F., Nelson, F., and Bockheim, J. 2001a. Patterns of soil temperature and moisture in the active layer and upper permafrost at Barrow, Alaska: 1993–1999, *Global and Planetary Change* **29**: 293–309.

Hinkel, K., Doolittle, J., Bockheim, J., Nelson, F., Paetzold, R., Kimble, J., and Travis, R. 2001b. Detection of Subsurface Permafrost Features with Ground-Penetrating Radar, Barrow, Alaska, *Permafrost Periglac. Process.* **12**: 179–190.

Ishikawa, M. 2003. Thermal regimes at the snow–ground interface and their implications for permafrost investigations, *Geomorphology* **52**:105–120.

Ishikawa, M., Watanabe, T. and Nakamura, N. 2001. Genetic difference or rock glaciers and the discontinuous mountain permafrost zone in Kanchanjunga Himal, eastern Nepal, *Permafrost and Periglacial Processes* **12**: 243–253.

Janke, J. 2005. Modeling past and future alpine permafrost distribution in the Colorado Front Range, *Earth Surface Processes and Landforms* **30**: 1495–1508.

Jorgenson, M., Racine, C., Walters, J., and Osterkamp, T. 2001. Permafrost degradation and ecological changes associated with a warming climate in central Alaska. *Climatic Change* **48**: 551–579.

Kakunov, N. 1999. Monitoring of the active/seasonally frozen layer and upper layers of cryolithozone during the ongoing half-century climatic cycle in the European northeast of Russia, *Abstracts of the International Conference 'Monitoring of Cryosphere' (Pushchino, Russia, 20–23 April 1999)*, 120–121.

Kneisel, C. 2006. Assessment of subsurface lithology in mountain environments using 2D resistivity imaging, *Geomorphology* **80**: 32–44.

Kneisel, C. and Hauck, C. 2003. Multi-method geophysical investigation of a sporadic permafrost occurrence, *Geophysical methods in geomorphology* **132**: 145–159.

Kneisel, C., Saemundsson, P., and Beylich A. 2007. Reconnaissance surveys of contemporary permafrost environments in central Iceland using geoelectrical methods: implications for permafrost degradation and sediment, *Geogr. Ann.* **89 A (1)**: 41–50.

Knopfle, W. 1999. Visualization of interferometric products derived from ERS1/2 tandom pair data, *IGARSS* **2**: 1378-1380.

Komarov, S., Mironov, V., and Li, S. 2002. SAR polarimetry for permafrost active layer freeze/thaw processes, *IGARSS*: 2654-2656.

Konrad, J.M. 1994. Sixteenth Canadian Geotechnical Colloquium: Frost heave in soils: concepts and engineering, *Canadian Geotechnical Journal*, **31:** 223-245.

Konrad, J.M. 1999. Frost susceptibility related to soil index properties, *Canadian Geotechnical Journal*, **36:** 403-417.

Krautblatter, M. and Hauck, C. 2007. Electrical resistivity tomography monitoring of permafrost in solid rock walls, *J. Geophys. Res*. **112**, F02S20,

Laberge, M. and Payette, S. 1995. Long-Term Monitoring of Permafrost Change in a Palsa Peatland in Northern Quebec, Canada: 1983-1993, *Arctic and Alpine Research* **27(2)**: 167-171.

Lachenbruch, A. and Marshall, B. 1986. Changing climate: geothermal evidence from permafrost in the Alaskan Arctic. *Science* **234**: 689–696.

Lanari, R., Fornaro, G., Riccio, D., Migliaccio, M., Papathanassiou, K., Moreira, J., Schwabisch, M., Dutra, L., Puglisi, G., Franceschetti, G., and Coltelli, M. 1996. Generation of digital elevation models by using SIR-C/X-SAR multifrequency two-pass interferometry: the Etna case study, *IEEE Transactions on Geoscience and Remote Sensing* **34(5)**: 1097-1114.

Laprise, D. and Payette, S. 1988. Evolution recente d'une tourbiere apalses (Quebec subarctique): Analyse cartographique et dendrochronologique, *Can. J. Bot.* **66:** 2217–2227.

Li, F. and Goldstein, R. 1990. Studies of multibaseline spaceborne interferometric synthetic aperture radars, *IEEE Trans.* **GE-28(1)**, pp 88-98.

Li, Z., Li, X., Ren, X. and Dong, Q. 2003. Frozen ground deformation monitoring using SAR interferometry, *Proc. IEEE* **4:** 2933 – 2935.

Little, J., Sandall, S., Walegur, M., and Nelson, F. 2003. Application of differential global positioning systems to monitor frost heave and thaw settlement in tundra environments, *Permafrost Periglac.* **14:** 349-357.

Lu, Z. and Freymueller, J. 1998. Synthetic aperture radar interferometry coherence analysis over Katmai volcano group, Alaska, *J. Geophys. Res.* **103:** 29,887–29,894.

Lu, Z., Power, J., McConnell, V., Wicks, C. and Dzurisin, D. 2002. Preeruptive inflation and surface interferometric coherence characteristics revealed by satellite radar interferometry at Makushin Volcano, Alaska: 1993–2000, *J. Geophys. Res.* **107(B11)**, ECV 1 1-13.

Mackay, J., Ostrick, J., Lewis, C., Mackay, D. 1979. Frost heave at ground temperatures below 0 8C, Inuvik, Northwest Territories, *Paper-Geological Survey of Canada* **79-1A**: 403–406.

Massonnet, D. and Feigl, K. 1995a. Satellite radar interferometric map of the coseismic deformation field of the *M* = 6*:*1 Eureka Valley California earthquake of May 17, 1993, *Geophys. Res. Lett.* **22:** 1541–1544.

Massonnet, D. and Feigl, K. 1995b. Discrimination of geophysical phenomena in satellite radar interferograms, *Geophys. Res. Lett.* **22:** 1537–1540.

Mauro, G. 2004. Observations on permafrost ground thermal regimes from Antarctica and the Italian Alps, and their relevance to global climate change. *Global and Planetary Change* **40**: 159–167.

Maxwell, B. 1997. Responding to global climate change in Canada's Arctic, *Volume II of the Canada Country Study: Climate impacts and adaptation.* Environment Canada.

Merry, C. 1998. Basics of Levelling. Lecture Series – University of Cape Town. Available at: http://64.233.167.104/search?q=cache:CPjeuX-qsCYJ:www.pol.ac.uk/psmsl/training/levelling.doc+Precise+levelling&hl=en&gl=ca&ct=clnk&cd=4

Miller, L., Hinkel, K., Nelson, F., Paetzold, R., Outcalt, S. 1998. Spatial and temporal patterns of soil moisture and thaw depth at Barrow, Alaska U.S.A. *Permafrost-Seventh International Conference* Universite Laval Centre d'etudes nordiques, Quebec, Canada, pp. 731–737.

Mironov, V., Komarov, S., Li, S., and Romanovsky, V. 2005. Freeze-thaw processes radar remote sensing: modeling and image processing. *IGARSS*: 608-611.

Moldoveanu, M., Stewart, R., Aitken, J., and Gallant, E. 2003. 3D Ground Penetrating Radar over ice and Permafrost, *CSEG*. Available at: www.crewes.org/Conference-abstracts/2003/SEG/Moldoveanu_SEG_2003.pdf

Moorman, B. and Vachon, P. 1998. Detecting ground ice melt with interferometric synthetic aperture radar, *20th Canadian Symposium on Remote Sensing*, Calgary, Alberta, May 10-13.

Muellerschoen, R., Chen, C., Hensley, S., and Rodriguez, E. 2006. Error Analysis for High Resolution Topography with Bi-static Single-Pass SAR Interferometry, *IEEE Conference on Radar* **8:** 626 – 633.

National Center for Atmospheric Research. 2005. Most Of Arctic's Near-surface Permafrost To Thaw By 2100, *ScienceDaily*. Retrieved January 20, 2008, from http://www.sciencedaily.com /releases/2005/12/051220085054.htm

Nelson, F. and Anisimov, O. 1993. Permafrost zonation in Russia under anthropogenic climate change, *Permafrost and Periglacial Processes* **4(2)**: 137-148.

Nelson, F., Hinkel, K., Shiklomanov, N., Mueller, G., Miller, L., Walker, D. 1998a. Active-layer thickness in north-central Alaska: systematic sampling, scale, and spatial autocorrelation, *Journal of Geophysical Research-Atmospheres* **103 (22):** 28963–28973.

Nelson, F., Outcalt, S., Brown, J., Shiklomanov, N., and Hinkel, K. 1998b. Spatial temporal attributes of the active-layer thickness record, Barrow, Alaska, USA, *7th International Conference on Permafrost*, Yellowknife, Canada. Centre d’e´tudes nordiques, Universite´ Laval, pp. 797– 802.

Nelson, F., Mueller, G., and Shiklomanov, N. 1999. Variability of active-layer thickness at multiple spatial scales, north-central Alaska, *U.S.A. Arctic, Antarctic, and Alpine Research* **31 (2)**: 158–165.

Nelson, F., Anisimov, O., and Shiklomanov, N. 2002. Climate Change and Hazard Zonation in the circum-arctic permafrost regions, *Natural Hazards* **26(3)**: 203-225.

Nelson, F. and Hinkel, K. 2003. Methods for Measuring Active-Layer Thickness. Available at: www.unis.no/RESEARCH/GEOLOGY/Geo_research/Ole/Periglacial Handbook/ActiveLayerThicknessMethods.htm

Nelson, F., Lachenbruch, A., Woo, M., Koster, E., Osterkamp, T., Gavrilova, M., and Cheng, G. 1993. Permafrost and Change Climate, *6th International Conference on Permafrost* **2:** 987-1005.

Nixon, F. and Taylor, A. 1998. Regional active layer monitoring across the sporadic, discontinuous and continuous permafrost zones, Mackenzie valley, northwestern Canada. *7th International Conference on Permafrost*, Yellowknife, Canada, pp. 815– 820.

Oberman, M. and Mazhitova, G. 2001. Permafrost dynamics in the north-east of European Russia at the end of the 20th century, *Norsk Geografisk Tidsskrift - Norwegian Journal of Geography* **55**:4, 241 – 244.

Osterkamp, T., Zhang, T. and Romanovsky, V. 1994. Evidence for a cyclic variation of permafrost temperature in northern Alaska, *Permafrost and Periglacial Processes* **5**: 137–144.

Ottesen, J., Galligan, D., Sterley, D., Burden, P., Wong, B., and Aho, J. 2002. An examination of resource transportation alternatives in Northwest Alaska, *Cold Regions Engineering Cold Regions Impacts on Transportation and Infrastructure: Proceedings of the Eleventh International Conference* p.182-193.

Pavlov, A. 1994. Current changes of climate and permafrost in the Arctic and sub-Arctic of Russia, *Permafrost & Periglacial Processes* **5(2)**: 101-110.

Payette, S., Delwaide, A., Caccianiga, M., and Beauchemin, M. 2004. Accelerated thawing of subarctic peatland permafrost over the last 50 years, *Geophys. Res. Lett*. **31**: L18208.

Pilon, J., Annan, A., Davis, J., and Gray, J. 1979. Comparison of thermal and radar active layer measurements in the Leaf Bay Area, Nouveau-Quebec, *Geographie Physique et Quaternaire* **23**: 317–326.

Pilon, J., Annan, A., and Davis, J. 1985. Monitoring permafrost ground conditions with ground probing radar (G.P.R.), *Workshop on Permafrost Geophysics, Golden, Colorado*, **CRREL Special Report 85-5**: 71–73.

Rankinen, K., Karvonen, T., and Butterfield, D. 2004. A simple model for predicting soil temperature in snow-covered and seasonally frozen soil: Model description and testing, *Hydrology and Earth System Sciences*, **8(4):** 706-716.

Rao, Y., Venkataraman, G., Rao, K., and Snehmani. 2004. SAR interferometry for DEM generation and movement of Indian glaciers, *IGARSS* **2**: 1128-1131.

Rodiguez, E. and Martin, J. 1992. Theory and design of interferometric synthetic aperture radars, *Pro. IEEE -F* **139(2)**: 147-159.

Romanovsky, V., Burgess, M., Smith, S., Yoshikawa, K., and Brown, J. 2002. Permafrost temperature records: indicators of climate change. *EOS, Transactions of the American Geophysical Union* **83**: 589, 593–594.

Rosen, P., Hensley, S., Zebker, H., Webb, F., and Fielding E. 1996. Surface deformation and coherence measurements of Kilauea volcano, Hawaii from SIR-C radar interferometry, *Journal of Geophysical Research* **101(E10):** 23109-23135.

Rosen, P., Hensley, S., Joughin, I., Li, F., Madsen, S., Rodriguez, E., and Goldstein, R. 2000. Synthetic Aperture Radar Interferometry, *IEEE* **88(3):** 333-382.

Salzmann, N., Frei, C., Vidale, P., and Hoelzle, M. 2007. The application of Regional Climate Model output for the simulation of high-mountain permafrost scenarios, *Global and Planetary Change* **56(1-2)**: 188-202.

Sardon, E., Rius, A., and Zarraoa, N. 1994. Estimation of the transmitter and receiver differential biases and the ionospheric total electron content from Global Positioning System observations, *Radio Science* **29(3)**: 577-586.

Scott, W., Sellmann, P., and Hunter, J. 1990. Geophysics in the study of permafrost, *Geotechnical and Environmental Geophysics, Vol. 1: Review and Tutorial*. Society of Exploration Geophysicists Investigation in Geophysics no. 5: 355–384.

Serreze, M., Walsh, J., Chapin, F., Osterkamp, T., Dyurgerov, M., Romanovsky, V., Oechel, W., Morison, J., Zhang, T., and Barry, R. 2000. Observational evidence of recent change in the northern high-latitude environment, *Climatic Change* **46**: 159–207.

Sheng, L., Tait, M., and Cannon, E. 2007. DGPS levelling and monument stability at 70 North, *Geomatica*. **61(1)**: 19-29.

SLAM (Services for Landslide Monitoring). 2006. Differential SAR Interferometry (DInSAR). Available online at: http://www.slamservice.info/methodology.asp

Smith, S., Burgess, M., Riseborough, D., and Nixon, F. 2005. Recent Trends from Canadian Permafrost Thermal Monitoring Network Sites, *Permafrost and Periglac. Process.* **16**: 19–30.

Stevens, N. and Wadge, G. 2004. Towards operational repeat-pass SAR interferometry at active volcanoes, *Natural Hazards* **33(1)**: 47-76.

Strozzi, T., Luckman, A., Murray, T., Wegmueller, U. and Werner, C. 2002. Glacier motion estimation using SAR offset-tracking procedures, *IEEE Transactions on Geoscience and Remote Sensing* **40(11)**: 2384-2391.

Strozzi, T., Wegmuller, U., Wiesmann, A,. Kaab, A., Frauenfelder, R., Werner, C., Graf, K., Ratzo, H., and Lateltin, O. 2003. Differential Interferometric Applications in Alpine Regions, *FRINGE Workshop*, Dec. 1-5, Frascati, Italy.

Swart, L. 2000. Spectral filtering and oversampling for radar interferometry, *Master's Thesis*, Faculty of Geodetic Engineering, Delft University of Technology.

Tait, M., and Moorman, B. 2003. A feasibility study into monitoring deformation in the Niglintgak region of the Mackenzie delta, *11th FIG Symposium on Deformation Measurement*, Santorini, Greece, May 25-29.

Tait, M., Sheng, L., and Cannon, E. 2004. The Feasibility of Replacing Precise Levelling with GPS for Permafrost Deformation Modelling, *INGEO and FIG Regional Central and Eastern European Conference on Engineering Surveying*, Bratislava, Slovakia.

Tait, M., Moorman, B., and Sheng, L. 2005. The long-term stability of survey monumentation in permafrost, *Journal of Engineering Geology* **79:** 61-79.

Tarayre, H. and Massonnet, D. 1994. Effects of a refractive atmosphere on interferometric processing, *IGARSS* 717–719.

Thie, J. 1974. Distribution and thawing of permafrost in the southern part of the discontinuous permafrost zone in Manitoba, *Arctic* **27:** 189– 200.

Ulaby, F., Moore, R., and Fung, A. 1986. Microwave Remote Sensing Active and Passive Volume 3. *Artech House Inc*. Norwood, MA.

U.S. Arctic Research Commission Permafrost Task Force. 2003. Climate Change, Permafrost and Impacts on Civil Infrastructure, *Special Report 01-03*, US Arctic Research Commission, Arlington , Virginia.

USINFO. 2005. Most Arctic Near-Surface Permafrost May Thaw by 2100, Study Finds, Available at: usinfo.state.gov/gi/Archive/2005/Dec/20-801705.html

Varner, C. and Cannon, E. 2002. Developing Carrier Phase Differential Global Positioning System Networks with Partial Derivative Algorithms, *Journal of Surveying Engineering* **128(2)**: 39-60.

Walker, G. 2007. Climate Change 2007: A world melting from the top down, *Nature* **446**: 718-221

Wang, Z. and Li., S. 1999. Detection of winter frost heaving of the active layer of Arctic permafrost using SAR differential interferograms, *Proc. IEEE* **4:** 1946-1948.

Wang, C., Zhang, H., Shan, X., Ma, J., Liu, Z., Chen, S., Lu, G., Tang, Y., and Guo, Z. 2004. Applying SAR Interferometry for Ground Deformation Detection in China, *Photogrammetric Engineering & Remote Sensing* **70(10)**: 1157-1165.

Wegmueller, U. and Werner, C. 1995. Farmland monitoring with SAR interferometry, *IGARSS*: 544-546.

Wegmueller, U., Werner, C., Strozzi, T. and Wiesmann, A. 2006. Application of SAR interferometric techniques for surface deformation monitoring, *3rd IAG/ 12th FIG* Symposium, Baden, Austria.

Wegmueller, U., Werner, C., Strozzi, T. And Wiesmann A. 2007. Gamma Remote Sensing SAR Software – trial version, *Gamma Remote Sensing AG*, Muri BE, Switzerland.

Williams, P. and Smith, M. 1989. *The Frozen Earth: Fundamentals of Geocryology*. Cambridge University Press, Cambridge.

Winter, D., Bergmann, D., Luehrig, B. and Ritter, R. 1993. Evaluation of ESPI phase images with regional discontinuities, *SPIE – The International Society for Optical Engineering* **2003**: 301-311.

Woodhouse, I. 2006. *Introduction to Microwave Remote Sensing*, Taylor & Francis, Florida.

Wong, J., Rossiter, J., Olhoeft, G., and Strangway, D. 1977. Permafrost: electrical properties of the active layer, *In situ. Canadian Journal of Earth Science* **14**: 582–586.

Zebker, H. and Goldstein, R. 1986. Topographic mapping from interferometric synthetic aperture radar observations, *J Geophys Res*..**91**: 4993-4999.

Zhang, T., Heginbottom, J., Barry, R., and Brown, J. 2000. Further statistics on the distribution of permafrost and ground ice in the northern hemisphere, *Polar Geography* **24**: 126–131.

Zhang, Y. and Cheng, X. 2005. Application of SRTM-DEM based two-pass SAR interferometry for detecting seismic deformation on high-altitude rugged terrain - A case study in Kokoxili Ms8.1 earthquake, 2001. *IGARSS* **7**: 5316-5319.

Zhang, Y. and Prinet, V. 2004. InSAR Coherence Estimation, *IGARSS* **5**: 3353-3355.

Zhen Li, Xinwu Li, Xin Ren, and Qin Dong. 2003. Frozen ground deformation monitoring using SAR interferometry, *IGARSS* **4**: 2933-2935.